



**HAL**  
open science

## **In-situ dissolution rates of silicate minerals and associated bacterial communities in the critical zone (Strengbach catchment, France)**

Bastien Wild, Damien Daval, Emilie Beaulieu, Marie-Claire Pierret, Daniel Viville, Gwenaël Imfeld

### ► **To cite this version:**

Bastien Wild, Damien Daval, Emilie Beaulieu, Marie-Claire Pierret, Daniel Viville, et al.. In-situ dissolution rates of silicate minerals and associated bacterial communities in the critical zone (Strengbach catchment, France). *Geochimica et Cosmochimica Acta*, 2019, 249, pp.95-120. 10.1016/j.gca.2019.01.003 . hal-02372322

**HAL Id: hal-02372322**

**<https://hal.science/hal-02372322>**

Submitted on 20 Nov 2019

**HAL** is a multi-disciplinary open access archive for the deposit and dissemination of scientific research documents, whether they are published or not. The documents may come from teaching and research institutions in France or abroad, or from public or private research centers.

L'archive ouverte pluridisciplinaire **HAL**, est destinée au dépôt et à la diffusion de documents scientifiques de niveau recherche, publiés ou non, émanant des établissements d'enseignement et de recherche français ou étrangers, des laboratoires publics ou privés.

1 *In-situ* Dissolution Rates of Silicate Minerals and  
2 Associated Bacterial Communities in the Critical Zone  
3 (Strengbach catchment, France)  
4

5 **Bastien Wild<sup>1,2</sup>, Damien Daval<sup>1</sup>, Emilie Beaulieu<sup>1</sup>, Marie-Claire Pierret<sup>1</sup>, Daniel Viville<sup>1</sup>,**  
6 **Gwenaël Imfeld<sup>1</sup>**

7 *<sup>1</sup>Laboratoire d'Hydrologie et de Géochimie de Strasbourg (LHyGeS), Université de*  
8 *Strasbourg /EOST-CNRS UMR 7517, 1 Rue Blessig, 67000 Strasbourg, France*

9 *<sup>2</sup>Andlinger Center for Energy and the Environment, Princeton University, Princeton, NJ*  
10 *08544, USA*

11 Corresponding author: [bwild@princeton.edu](mailto:bwild@princeton.edu)

25        **ABSTRACT**

26        Weathering of silicate minerals in the Critical Zone (CZ) is fundamental for numerous  
27 environmental and societal issues. Despite decades of efforts to accurately record  
28 biogeochemical variables controlling mineral reactivity in the field and to reproduce them in  
29 the laboratory, weathering rates estimates still differ from those observed in natural settings.  
30 Here we examine the biogeochemical environment of mineral surfaces exposed to contrasted  
31 weathering conditions in various compartments of a temperate CZ (Strengbach observatory,  
32 France). A novel approach was developed to probe both *in-situ* mineral dissolution rates and  
33 bacterial diversity associated to mineral surfaces. Labradorite and olivine minerals were either  
34 buried in the A and C horizons of a soil profile, directly exposed to meteoric fluids or immersed  
35 in stream water. Dissolution rates recorded in the soil profile were up to 2 orders of magnitude  
36 slower than those predicted using a numerical weathering model. Samples directly exposed to  
37 meteoric fluids exhibited contrasted dissolution rates that could not be explained by simple  
38 abiotic weathering, while dissolution rates of samples incubated in stream water were  
39 particularly low. In soil profiles, the field-laboratory discrepancy by up to 2 orders of magnitude  
40 was attributed to heterogeneity of fluid circulation and local variation of reaction conditions.  
41 Mineral substrates changed bacterial communities of the mineralosphere after 9 and 20 months  
42 of incubation in the CZ. However, we observed that this effect could be delayed or driven by  
43 extrinsic factors. Although mineral probes in soil horizons were enriched in bacterial  
44 phylotypes potentially involved in mineral weathering (e.g., *Pseudomonas* sp., *Collimonas* sp.,  
45 *Burkholderia* sp., *Janthinobacterium* sp., *Leifsonia* sp., and *Arthrobacter* sp.), the relative  
46 contribution of biotic weathering could not be quantified *in-situ*. Altogether, the heterogeneity  
47 of *in-situ* mineral dissolution rates in key compartments of the CZ reveals the crucial need to  
48 improve spatial characterization of hydrogeochemical properties at the soil profile scale, and to  
49 evaluate the quantitative role of microbial communities to mineral weathering.

## 50 1. INTRODUCTION

51 Weathering of primary minerals and associated fluxes involved in elemental cycling in  
52 natural settings are relevant for numerous environmental and societal challenges. Important  
53 issues include the management of inorganic nutrients stocks in soils with the development of  
54 sustainable agricultural and forestry practices (Johnson et al., 2015; Klaminder et al., 2011;  
55 Lucas et al., 2011; van der Heijden et al., 2013), the contamination of ecosystems due to mining  
56 activities (Yu et al., 2014), or long-term forecast of atmospheric CO<sub>2</sub> concentrations (Beaulieu  
57 et al., 2012).

58 Studies on (bio)weathering rates at global (Gaillardet *et al.*, 1999), regional (Gaillardet *et*  
59 *al.*, 1995; Negrel *et al.*, 1993), local (Augusto *et al.*, 2000; Feger *et al.*, 1990; Klaminder *et al.*,  
60 2011) or micro scales (Bonneville *et al.*, 2016; Fischer *et al.*, 2012; Li *et al.*, 2016) underscore  
61 that the knowledge of mineral dissolution rates in the critical zone (CZ) remains incomplete.  
62 Field weathering rates are usually determined with indirect methods, such as measurements of  
63 U-series nuclides in soils and weathering profiles (Ackerer et al., 2016), the monitoring of  
64 changes in solid-state regolith compositions (White et al., 1996) and/or geochemical mass-  
65 balances over large space and time scales (Velbel, 1993). These rates are often inconsistent with  
66 those measured in the laboratory (White and Brantley, 2003). This “field-lab discrepancy”  
67 (Paces, 1983; White and Brantley, 2003; Zhu *et al.*, 2014) has stimulated intensive research to  
68 reduce uncertainties on element budgets in natural settings. For instance, several types of  
69 indirect field measurement approaches were combined to yield estimates of *in-situ* mineral  
70 weathering rates (Ackerer *et al.*, 2016; Ferrier *et al.*, 2010). In parallel, mineral dissolution  
71 kinetics were evaluated in the laboratory by monitoring dissolution rates against controlled  
72 parameters, such as T, pH or  $\Delta G_r$  (Carroll and Knauss, 2005; Gruber et al., 2014; Hellmann  
73 and Tisserand, 2006). This framework allowed to build up databases of parameters used in  
74 semi-empirical mineral weathering rate laws (Palandri and Kharaka, 2004; Rimstidt *et al.*,

75 2012). While this overall strategy has the merit to combine data from independent “top-down”  
76 (field measurements) and “bottom-up” (lab experiments) approaches, a consistent theory for  
77 mineral weathering in the field is still missing. One possible reason is that “top-down” and  
78 “bottom-up” approaches consider different processes, which are recorded on distinct temporal  
79 and spatial scales.

80 Most field studies integrate mineral weathering over large space scales, which do not  
81 capture the details of the biogeochemical processes at stake. Field studies may thus fail to  
82 provide a mechanistic understanding of *in-situ* mineral weathering, although relevant data for  
83 past and current weathering in the critical zone have been produced. Estimates of field  
84 weathering rates remain, however, several orders of magnitude greater than laboratory  
85 estimates that feed common rate laws used in reactive transport models (Maher et al., 2004;  
86 White and Brantley, 2003).

87 In addition, inconsistent timescales considered in the laboratory and in the field may result  
88 in contrasted mineral dissolution rates due to intrinsic factors, i.e. related to the intrinsic crystal  
89 chemistry of the weathered phase, or extrinsic factors, i.e. related to the reacting environment  
90 of the crystal (Beig and Luttge, 2006; Gruber et al., 2014; White and Brantley, 2003). Indeed,  
91 the physicochemical properties of the fluid/silicate interface may change over time during  
92 mineral dissolution, depending on weathering conditions (Daval et al., 2011; Wild et al., 2016).  
93 As a result, the dissolution rate of mineral surfaces aged over geologic time scales in the field  
94 cannot be directly compared to that of pristine mineral surfaces used in the laboratory, resulting  
95 in inconsistent estimates of mineral weathering rates. Moreover, silicate mineral dissolution is  
96 too slow under typical field conditions to be measured directly with sufficient accuracy. As a  
97 result, most studies on silicate dissolution kinetics have been restricted to the investigation of  
98 abiotic, far-from-equilibrium conditions (extreme pH and/or temperature conditions) in

99 laboratory setups. These experimental conditions might change the nature of the elementary  
100 processes actually driving mineral dissolution compared to those prevailing in the field.

101 To sum up, (i) mineral dissolution rates measured in the field and in the lab over contrasted  
102 time and space scales may not account for the same processes, (ii) local physicochemical  
103 environments controlling mineral dissolution rates in the CZ can hardly be probed, and (iii)  
104 laboratory conditions, which are generally controlled, homogeneous, constant and abiotic (or  
105 which do not involve (multiple) (micro)organisms), might only partly reflect processes ongoing  
106 in the field. In that sense, the strict addition of numerous processes observed independently in  
107 simple laboratory set-ups (e.g., abiotic, high temperature, short timescales, etc.) may fail to  
108 reproduce mineral weathering in natural settings. Nevertheless, parameters derived from  
109 laboratory experiments are directly used in reactive transport codes (Gerard *et al.*, 1996; Steefel  
110 and Lasaga, 1994; Yeh and Tripathi, 1991) or in chemical weathering models at the catchment  
111 scale (Godderis *et al.*, 2006; Sverdrup and Warfvinge, 1995). Current models may thus partly  
112 fail to account for extrinsic and intrinsic processes, possibly resulting in a limited agreement  
113 between simulation outputs and measurements of field weathering rates.

114 While several models integrate element recycling by vegetation and soil acidity controlled by  
115 heterotrophic and autotrophic respiration (Beaulieu *et al.*, 2012; Godderis *et al.*, 2006; Roelandt  
116 *et al.*, 2010), the influence of microorganisms on *in-situ* mineral dissolution is currently  
117 missing. However, microorganisms have been recognized to interact with mineral substrates  
118 (Bennett *et al.*, 1996; Uroz *et al.*, 2009; Uroz *et al.*, 2015), and to impact mineral weathering  
119 directly or indirectly. For instance, microorganisms can control locally the thermodynamic  
120 activity of species in solution by biofilm production (Barker and Banfield, 1996) or produce  
121 organic molecules (either organic acids, ligands or siderophores), which may result in organic-  
122 metal chelation (Drever and Stillings, 1997) or ligand-promoted dissolution (Ganor *et al.*, 2009;  
123 Welch and Ullman, 1993). Microorganisms can also impact mineral weathering by modifying

124 redox (Lower *et al.*, 2001; Newman and Kolter, 2000; Reguera *et al.*, 2005; Roden *et al.*, 2010)  
125 or acid-base conditions (Alisa Mast and Drever, 1987), or even by inducing mechanical stress  
126 (Bonneville *et al.*, 2009; Li *et al.*, 2016). The effect of individual microbial strains on mineral  
127 weathering has been extensively characterized in controlled systems (Brantley *et al.*, 2001;  
128 Kalinowski *et al.*, 2000). However, this approach relies on the selection of culturable strains,  
129 which accounts for much less than 1% of the microorganisms occurring in many environments  
130 (Solden *et al.*, 2016). Some model microorganisms may thus be selected based on cultivation  
131 restrictions (van Scholl *et al.*, 2008) rather than for their actual effect or relevance for mineral  
132 weathering. To date, most available bioweathering studies have been considering axenic  
133 cultures, with the exception of some recent attempts to use field-relevant microbial  
134 communities (Wild *et al.*, 2018). In addition, planktonic cells are generally considered, while  
135 biofilms, are often neglected in weathering studies. Altogether, this questions the environmental  
136 relevance of experiments conducted with model cultures to infer weathering rates under field  
137 conditions. Identifying the weathering potential of microbial communities, as well as their  
138 contribution to global weathering fluxes, remains a challenging but fundamental issue that  
139 remains largely unexplored.

140 Another important gap between laboratory and field conditions is the consideration of  
141 microbial communities in nutrient-poor environments. While microorganisms influence  
142 mineral dissolution rates, the mineral substratum may reciprocally influence microbial  
143 communities {Bennett, 2001; Certini, 2004; Gleeson, 2005; Gleeson, 2006; Mitchell, 2013;  
144 Rogers, 2004; Uroz, 2012; Wild, 2018}. Minerals can thus constitute an ecological niche called  
145 the mineralosphere (Uroz *et al.*, 2015). However, factors controlling the interplay between  
146 microbial composition and mineral weathering in natural settings remain poorly known.

147 In this context, the purpose of this study was to evaluate *in-situ* mineral dissolution rates in  
148 key compartments of the CZ, to assess the physicochemical parameters controlling the

149 dissolution process and to evaluate its impact on bacterial communities. We incubated *in-situ*  
150 fresh mineral powders and polished surfaces (i.e., prepared in the laboratory) directly in  
151 environmental settings. This approach attempts to bridge field and laboratory measurements by  
152 probing *in-situ* (or “on site”) field weathering rates, and by integrating all biotic and abiotic  
153 factors contributing to silicate mineral weathering in the field. Mineral dissolution and bacterial  
154 communities associated to different types of silicates (see section 2.1) were directly probed in  
155 different compartments of the Strengbach Critical Zone Observatory (CZO, Eastern France).  
156 Targeted compartments included (i) rocks in open-air weathering conditions (i.e., direct  
157 exposure to meteoric fluids), (ii) two contrasted soil compartments (A and C soil horizons), and  
158 (iii) the Strengbach stream at the outlet of the watershed. Direct field estimates of mineral  
159 weathering rates were compared to rates predicted with the WITCH model (Godderis *et al.*,  
160 2006) relying on dissolution rate laws derived from laboratory measurements. This enabled to  
161 identify factors contributing to the field-laboratory discrepancy. In parallel, bacterial 16S rRNA  
162 gene surveys were conducted using high-throughput sequencing to explore the diversity of  
163 microbial communities associated to weathered minerals. Amongst all possible actors for  
164 microbial weathering, we focus here on bacteria, whose role in mineral weathering have already  
165 been extensively described in literature (see, e.g. Uroz *et al.*, 2015 for a review).

166

## 167 **2. METHODS**

### 168 **2.1. Mineral selection**

169 Labradorite, olivine and quartz were selected for this study as model minerals. Labradorite  
170 is a tectosilicate belonging to the plagioclase feldspar series, which prevails in the continental  
171 crust. Labradorite is a rather reactive feldspar with an approximately halfway composition  
172 between albite and anorthite end-members. It contains Na, Ca and some K cations, whose pools  
173 may be threatened by some forestry practices in temperate forest ecosystems (Johnson *et al.*,



174 2015; Lucas *et al.*, 2011; van der Heijden *et al.*, 2013). The labradorite used in this study  
175 originates from Madagascar and has the following average composition:  $\text{Na}_{0.5}\text{Ca}_{0.5}\text{Al}_{1.5}\text{Si}_{2.5}\text{O}_8$   
176 (Wild *et al.*, 2016). The olivine used here originates from San Carlos and has a composition  
177 close to the pure forsterite pole ( $\text{Fo}_{92.0\pm 1.3}$ ), as determined by inductively coupled plasma atomic  
178 emission spectroscopy (ICP-AES) after a standard lithium metaborate fusion. Olivine is a  
179 nesosilicate that is characteristic of mafic to ultramafic geological settings. While this mineral  
180 is exogenous to the geological context of the study site, it contains Fe and Mg, which are  
181 relevant micronutrients in forest ecosystems, and especially for the Strengbach catchment. Fe  
182 is a limiting nutrient in most of aerobic natural settings (Johnstone and Nolan, 2015) due to its  
183 rapid oxidation kinetics (Davison and Seed, 1983) and its low bioavailability (Saha *et al.*,  
184 2013). Deficiency in bioavailable Mg has been reported for the Strengbach CZ (Bonneau *et al.*,  
185 1991; Dambrine *et al.*, 1992). Quartz was provided by the Museum of Mineralogy of Strasbourg  
186 (France). Quartz is nutrient-free, and it was used in parallel as a non-weatherable reference  
187 under the reacting conditions and over the time scales considered (Knauss and Wolery, 1988;  
188 Tester *et al.*, 1994).

189

## 190 **2.2. Study site**

191 Mineral samples were incubated at the Strengbach catchment (Observatoire  
192 Hydrog ochimique de l'Environnement, Alsace, France; 48°12'48.33''N; 7°12'2.23''E, 1146  
193 m (summit) to 883 m (outlet)), involved French and international critical zone observatories  
194 networks (OZCAR, <http://www.ozcar-ri.org/>; RBV,  
195 <http://portailrbv.sedoo.fr/?locale=en#CMSConsultPlace:HOME>; CZEN,  
196 <http://www.czen.org/content/strengbach-catchment-ohge>). The Strengbach stream drains a  
197 surface area of 80 ha (Fig. 1 A). Forested land comprises 80 % of conifers (*Picea abies*), and  
198 20% of lobed-leaved trees, dominated by *Fagus sylvatica* spp.

199 The watershed lies on a granitic bedrock, mainly composed of a Hercynian base-poor  
200 granite (cordieritic granite) with low Ca and Mg contents, which has been strongly  
201 hydrothermally altered on the northern slope and comparatively weakly altered on the southern  
202 slope. The top of the northern slope is covered by a 20 to 30 m -thick gneiss layer. Several  
203 microgranite intrusions occurred in the southern face (El Gh'Mari, 1995; Pierret *et al.*, 2014).

204 The soils of the watershed range from ochre podzolic soils to brown acidic soils (Lefèvre,  
205 1988). Since 1985, the OHGE is fully equipped for continuous monitoring of climatic and  
206 hydrogeochemical parameters (Pierret *et al.*, 2014; Viville *et al.*, 2012). Climatic data were  
207 obtained from a weather station (Fig. 1 A).

208 The pedological parameters of 10 soil samples collected at the beech plot on 11/18/2013  
209 and 12/02/2014 were analyzed at INRA, Arras, France (Tables A.1-A.4; Fig. 1B). About 1 kg  
210 of soil samples was collected at several depths along a 120 cm depth soil profile. Water content  
211 was estimated by weighing samples before and after drying at 110°C. Soil samples were  
212 quartered and sieved (2 mm) as described in previous studies (Duplay *et al.*, 2014; Lucas *et al.*,  
213 2011). Granulometry and organic fractions were determined according to SOL-0303 and SOL-  
214 0401 standardized procedures, respectively.

215

### 216 **2.3. Experimental setting**

217 Two sets of mineral probes were incubated simultaneously into four contrasted  
218 compartments of the CZ (atmosphere, A and C soil horizons and stream). The mineral probes  
219 were collected separately after 9 and 20 months to evaluate temporal changes. Each set of  
220 probes consisted of two types of probes: (i) the integrative reactivity probes to estimate *in-situ*  
221 dissolution rates of labradorite, olivine and quartz, and (ii) the environmental probes to  
222 characterize bacterial communities associated to each mineral.

223

224        2.3.1. *Integrative reactivity probes*

225        The integrative reactivity probes consisted of fresh mineral surfaces of labradorite and  
226        olivine prepared by polishing raw materials to eliminate the impact of surface ageing on surface  
227        reactivity. A Room Temperature Vulcanizing (RTV) glue mask was deposited on each polished  
228        surface to enable direct measurements of the mean mineral weathering rates *in-situ*, integrated  
229        over the incubation time, by comparing the topography of the mineral sample before and after  
230        incubation (Wild *et al.*, 2016; see also section 2.4). Reactivity of samples is quantified in terms  
231        of surface-normalized dissolution rates ( $\text{mol.m}^2.\text{s}^{-1}$ ) throughout this article.

232        Samples were cleaned with ethanol and packed into 100  $\mu\text{m}$ -calibrated mesh nylon cloth  
233        (Fisher Scientific, Pittsburgh, PA) to allow circulation of soil fluids and microorganisms. Each  
234        nylon bag was individually sealed by sewing with 0.12 mm nylon thread. Bags were sterilized,  
235        and DNA was eliminated under UV light and rinsed with 0.2- $\mu\text{m}$  filtrated ethanol. Bags were  
236        then dried under laminar flow and kept sterile until incubation at the Strengbach catchment (see  
237        Fig. 1-A, and section 2.3.3).

238

239        2.3.2. *Environmental probes*

240        The environmental probes consisted of nylon bags filled up with sterile labradorite, olivine  
241        and quartz powders for bacterial colonization. Powder preparation and sterilization was  
242        performed as described in Wild *et al.* (2016) and Wild *et al.* (2018). Briefly, olivine, labradorite  
243        and quartz crystals were crushed with a hydraulic press, and the powder was dry sieved to  
244        recover the 160-315  $\mu\text{m}$  fraction (Fig. A.1). Residual fine particles were removed by successive  
245        sonication steps in ethanol, and the removal of particles was assessed by SEM observations.  
246        The specific surface area of powders was measured using the Brunauer-Emmet-Teller method  
247        (BET, Brunauer *et al.*, 1938). Powders were washed for 10 minutes in sterile vessels with two  
248        successive baths of 0.2  $\mu\text{m}$  filtered absolute ethanol, dried for >60 min under sterile laminar

249 flow and exposed to ultraviolet radiation for 20 min. A known amount of powder (2.5-3.5 g)  
250 was then sealed in a nylon bag allowing circulation of environmental fluid and microorganisms.  
251 Environmental probes were further cleaned and sterilized prior to their incubation at the  
252 Strengbach catchment as described previously. Empty control bags were added to each set to  
253 evaluate the effect of the nylon bag on bacterial communities.

254

### 255 *2.3.3. Incubation of the probes in CZ compartments*

256 A first set of probes was fixed to a perforated Polytetrafluoroethylene (PTFE) plate allowing  
257 rainfall to flow across the nylon bags (Fig. 1E and 1F). Probes were placed at the weather station  
258 (Fig. 1A; 48°13'0.56"N; 7°11'47.82"E). Samples were directly exposed to atmospheric  
259 weathering (wind, rainfall and meteoric deposits). This "meteoric" compartment represents the  
260 entry point at the atmosphere-soil interface of the CZ, which is not influenced by soil  
261 hydrological or pedogenesis processes.

262 Two other sets of probes were incubated into the A-horizon (10-cm depth) and the C-  
263 horizon (>60 cm) of the soil profile (Fig. 1B) of the reference beech plot (48°12'41.04"N;  
264 7°11'45.66"E). This plot was selected as it combines higher rainfall volumes (northern slope),  
265 simple topography (single slope, Fig. 1A) and homogeneous soil and forest covers. Incubation  
266 depths corresponded to that of zero-tension lysimetric plates collecting soil solutions since  
267 1992. Mean pH of solutions from A-horizon was  $4.22 \pm 0.17$  (1992-2016 period,  $n = 178$   
268 measurements). In the C horizon, a lower dissolution rate is expected due to higher pH values  
269 (mean  $\pm$  SD:  $4.89 \pm 0.28$ ; 1992-2016 period,  $n = 104$  measurements). Overall, hydrological,  
270 geochemical and microbial processes at the A-horizon (topsoil, leaf litter) and the C-horizon  
271 (saprolite) are expected to differ.

272 The fourth set was incubated in the Strengbach stream, at the outlet of the watershed  
273 (48°13'0.56"N; 7°12'20.95"E), to allow for a permanent fluid-mineral contact. Samples were

274 inserted into PTFE tubes and oriented along stream flow (Fig. 1H and 1I). The average pH of  
275 the stream measured at the outlet was  $6.46 \pm 0.24$  for the period of incubation (2014/2015).

276 The sets of probes were collected separately after 9 months (from March 3<sup>rd</sup>, 2014 to  
277 December 2<sup>nd</sup>, 2014) and 20 months (from March 3<sup>rd</sup>, 2014 to November 9<sup>th</sup>, 2015) using sterile  
278 forceps. The probes were individually placed into sterile 50 mL Falcon tubes and transported  
279 into the laboratory in a sealed cooler and further handled under sterile laminar flow. Probes  
280 were collected during the same season (fall) to limit seasonal effects on microbial communities  
281 of the mineralosphere (Uroz *et al.*, 2011).

282

#### 283 **2.4. Measurement of mineral weathering rates**

284 Vertical scanning interferometry (VSI, Zygo New View 7300) was used to estimate mineral  
285 weathering rates  $r$ , based on the global retreat ( $\Delta z$ ) of the surface of each integrative reactivity  
286 probe after incubation, compared to an unreacted (masked) portion of the same mineral surface,  
287 as follows:

$$r = \frac{\Delta z}{\Delta t * V_m} \quad (1)$$

288 where  $\Delta t$  stands for the incubation duration and  $V_m$  is the molar volume of the considered  
289 mineral. This approach was previously shown to provide dissolution rates consistent with  
290 classical powder dissolution experiments (Arvidson *et al.*, 2003; Arvidson and Luttge, 2010;  
291 Daval *et al.*, 2013), and has been applied here for the first time in the field.

292

#### 293 **2.5. Predictions of mineral weathering rates**

294 The WITCH model (Godderis *et al.*, 2006) was used to evaluate mineral dissolution rates  
295 of samples incubated in soils. The model used physicochemical parameters recorded *in-situ*  
296 during mineral incubation. WITCH enabled to reproduce *in-situ* reactivity conditions (e.g.  
297 parameters of the reactive fluids including T, pH and more generally, solution composition) at

298 stake during probe incubation using the OHGE database (1987-2016). Modeled mineral  
299 dissolution rates relying on kinetic rate laws derived from previous laboratory weathering  
300 experiments were compared to *in-situ* measurements based on integrative reactivity probes  
301 (field rates). Input parameters of WITCH model such as the solubility products of secondary  
302 phases were previously adjusted in a wide variety of contexts (Beaulieu et al., 2012; Beaulieu  
303 et al., 2010; Godderis et al.; Violette et al., 2010). Therefore, differences between modeled and  
304 observed dissolution rates were interpreted here in terms of field-lab discrepancy.

305 Briefly, the model considered a one-dimensional soil profile discretized into 36  
306 homogeneous boxes of 5-cm height overlying a bedrock layer. At each time step, the code  
307 solves the following mass-balance equation for each box:

$$\frac{dC}{dt} = F_{up} - F_{down} + F_{weath} - F_{prec} + F_{ex} + F_{veg} \quad (2)$$

308 where  $C$  is the concentration of a given dissolved species in the considered box.  $F_{up}$  represents  
309 the input flux at the top of the considered box through drainage while  $F_{down}$  is the output flow  
310 through downward drainage.  $F_{weath}$  and  $F_{prec}$  stand for the release of a given species from  
311 primary minerals through weathering processes or for its consumption by the precipitation of  
312 secondary phases, respectively.  $F_{ex}$  and  $F_{veg}$  stand for the fluxes associated to the exchange of  
313 this species with the argilo-humic complex or with the vegetation (either nutrient consumption  
314 or organic matter decay), respectively. Input fluxes were estimated by a series of rain gauges  
315 and an experimental setup at the beech plot dedicated to throughfall and soil solution collection  
316 (Prunier *et al.*, 2015, <http://ohge.unistra.fr/>). Output elemental fluxes from the watershed were  
317 quantified by an experimental hutch located at the catchment outlet, where water discharge,  
318 solute concentrations, suspended matter and sediments are continuously quantified (Viville *et*  
319 *al.*, 2012). Fluxes related to mineral weathering were calculated as follows:

$$F_{weath} = Area_{Min} * \phi_{Min} * SMS * x_{molar} * R_{min} \quad (3)$$

320 where  $Area_{Min}$  corresponds to the mineral specific surface area in  $m_{mineral}^2 \cdot m_{soil}^{-3}$ ,  $\phi_{Min}$  stands  
 321 for the volumetric proportion of that mineral in the considered soil horizon,  $x_{molar}$  is the  
 322 stoichiometric coefficient of the element of interest in the considered mineral.  $SMS$  refers to  
 323 the soil moisture saturation (Sverdrup, 1990; Sverdrup and Warfvinge, 1993; Warfvinge and  
 324 Sverdrup, 1992):

$$SMS = \frac{\theta * \rho_{solid}}{\rho_{solid} - \rho_i + \theta * \rho_{water}} \quad (4)$$

325 where  $\rho_{solid}$  and  $\rho_{water}$  are the density of the soil particles and water respectively ( $kg \cdot m^{-3}$ ),  $\rho_i$   
 326 is the bulk density of the soil and  $\theta$  is the dimensionless soil water content. The water content  
 327 of each soil layer and the vertical drainage used by the WITCH model were estimated using the  
 328 BILJOU© model (Granier *et al.*, 1999).

329  $R_{min}$  ( $mol \cdot m^{-2} \cdot s^{-1}$ ) is the mineral weathering rate defined as:

$$R_{min} = \left[ \sum_i A_{i,min} \cdot \exp\left(\frac{-E_{a,min}^i}{RT}\right) \cdot a_i^{n_{i,min}} \right] (1 - \Omega^S) \quad (5)$$

330 where  $A_{i,min}$  ( $mol \cdot m^{-2} \cdot s^{-1}$ ) is the Arrhenius pre-exponential factor,  $R$  ( $J \cdot mol^{-1} \cdot K^{-1}$ ) the  
 331 gas constant and  $T$  ( $K$ ) the absolute temperature, respectively.  $E_{a,min}^i$  ( $J \cdot mol^{-1}$ ) is the activation  
 332 energy,  $a_i$  the dimensionless ion activity and  $n_{i,min}$  the dimensionless reaction order with  
 333 respect to the hydrolysis of mineral  $min$  by the reactive species  $i$  (either  $H^+$ ,  $OH^-$ ,  $H_2O$  or an  
 334 organic ligand).  $\Omega$  is the dimensionless mineral saturation index and  $S$  is a dimensionless  
 335 empirical fitting parameter (Maher *et al.*, 2009) assimilated to a “stoichiometric number”  
 336 (Godd ris and Donnadieu, 2009; Godderis *et al.*, 2006) equal to 1 for olivine and to 1/3 for  
 337 labradorite according to the WITCH database.

338 The soil mineral specific surface area was estimated from soil texture according to a  
 339 parametric law (Sverdrup and Warfvinge, 1995):

$$Area_{Min} = \rho * (8.0 * X_{clay} + 2.2 * X_{silt} + 0.3 * X_{sand}) \quad (6)$$

340 where  $\rho$  is the density of the considered soil layer, and  $X_{clay}$ ,  $X_{silt}$ , and  $X_{sand}$  correspond to the  
341 clay, silt and sand fraction, respectively, with

$$X_{clay} + X_{silt} + X_{sand} = 1 \quad (7)$$

342 Soil texture (different fractions), density and porosity were measured on-site for the superficial  
343 and the deep layers (5- and 150 cm-depth respectively). The average composition of top and  
344 deep soil layers considered to run simulations were: 15% clay, 19% silt and 66% sand, and 9%  
345 clays, 19% silt and 72% sand, respectively (according to Table A.2 and Beaulieu *et al.*, 2016).  
346 The mineralogical composition in each box was calculated by linear interpolation of the  
347 measured data given above. The relative proportions of olivine and labradorite ( $\phi_{olivine}$  and  
348  $\phi_{Labradorite}$ ) were set to 0.001% to make sure that their contribution to the modeled solution  
349 composition remains negligible. The flux of exchangeable ions ( $Ca^{2+}$ ,  $Mg^{2+}$ ,  $K^+$ ,  $SO_4^{2-}$ ,  
350  $HPO_4^{2-}$ ,  $Al^{3+}$  et  $Na^+$ ) was defined following a Fickian diffusion law:

$$\frac{dE_{EC}}{dt} = -k_x(EC_{surf} - EC_{sol}) \quad (8)$$

351 where  $E_{EC}$  is the fraction of sites occupied by an exchangeable ion  $EC$ , and  $k_x$  is a mass transfer  
352 coefficient determined according to the literature (Warfvinge and Sverdrup, 1988).  $EC_{sol}$  and  
353  $EC_{surf}$  are concentrations calculated in the bulk solution and at the surface of the argilo-humic  
354 complex, respectively, based on data from the literature (Alveteg, 1998). Element exchanges  
355 between vegetation and soil ( $F_{veg}$ ) were estimated based on carbon net primary production and  
356 carbon recycling determined by the Lund-Potsdam-Jena (LPJ) dynamic global vegetation  
357 model (Sitch *et al.*, 2003), and from element/carbon ratios established by Redfield (see Drever  
358 *et al.*, 1997). Plant nutrient uptake was allowed down to 1.5 m depth (root compartment),  
359 whereas elemental release from litter degradation was only allowed in the superficial soil  
360 horizon (above 0.5 m depth) (Beaulieu *et al.*, 2012; Beaulieu *et al.*, 2010; Roelandt *et al.*, 2010).  
361 Soil acidification from carbon dioxide partial pressure ( $p_{CO_2}$ ) induced by autotrophic and



362 heterotrophic respiration processes were calculated from climatic data (precipitation,  
363 temperature, cloud cover, atmospheric  $CO_2$  concentration) sourced from the OHGE and CRU-  
364 TS global databases (Harris *et al.*, 2014). The actual chemical composition of the input solutions  
365 (throughfall) as a boundary condition at the top of the soil column at each time step was  
366 determined using the dynamic version of the code. The model was calibrated using time series  
367 from 1987 to 2015 and comparison of the composition of soil solutions collected from the  
368 lysimetric plates with those predicted at the corresponding depth (see Tables A.5 and A.6).  
369 Sulfate concentration, which only depends on hydrological parameters due to the absence of  
370 weatherable sulfate-bearing phases at the Strengbach watershed, were reproduced for the A-  
371 horizon (Table A.5). The temperature profile along the soil column was defined for each box  
372 by linear interpolation between surface temperature and temperature at 1.5 m-depth, defined at  
373 each time step as the gliding annual mean of surface temperatures.

374 For mineral samples immersed in the Strengbach stream and at the weather station,  
375 predicted surface retreats were estimated assuming permanent contact of the mineral with a  
376 solution at a pH corresponding to the annual average pH of the stream or of the rainfall,  
377 respectively. The solution-mineral interaction was assumed to be constant throughout the  
378 incubation period at a temperature corresponding to the annual mean water and air temperature,  
379 respectively.

380

## 381 **2.6. Bacterial community analysis**

### 382 *2.6.1. DNA extraction*

383 Total DNA was extracted from the soil samples and the stream sediments with a PowerSoil<sup>®</sup>  
384 DNA Isolation Kit (MO BIO, Carlsbad, CA, USA) following manufacturer's instructions. DNA  
385 extraction were performed on single samples due to limited quantities of incubated powder. The  
386 concentrations of DNA were determined using a Qubit<sup>®</sup> Fluorometer and Qubit<sup>®</sup> dsDNA HS

387 Assay Kit (Invitrogen, Carlsbad, CA, USA). A DNA extraction was first carried out from sterile  
388 mineral powder before incubation in the CZ compartment. DNA could not be detected in sterile  
389 and cleaned samples. Concentrations of DNA extracted from incubated probes ranged from 0.1  
390 to 2.1 ng. $\mu\text{L}^{-1}$  for the atmospheric probes, 0.6 to >6 ng. $\mu\text{L}^{-1}$  for the A-horizon probes, 0.1 to >6  
391 ng. $\mu\text{L}^{-1}$  for the C-horizon probes, and 3.69 to >6 ng. $\mu\text{L}^{-1}$  for the stream probes.

392

### 393 *2.6.2. Illumina MiSeq sequencing and data processing*

394 The sequencing procedure has been described previously (Babcsanyi et al., 2017).  
395 Sequencing was performed at the Research and Testing Laboratory (Lubbock, TX, USA) using  
396 Illumina MiSeq. The 16S rRNA gene spanning hypervariable region V4 was amplified in a  
397 two-step process. Forward primer was based on illumina i5 primer (5'-  
398 TCGTCGGCAGCGTCAGATGTGTATAAGAGACAG-3') the universal bacterial 515F  
399 primer (5'-GTGCCAGCMGCCGCGGTAA-3') (Walters et al., 2011). Corresponding reverse  
400 primer was synthesized from illumina i7 primer (5'-  
401 GTCTCGTGGGCTCGGAGATGTGTATAAGAGACAG-3') and universal bacterial primer  
402 806R (5'-GGACTACHVGGGTWTCTAAT-3'). Sequences were generated by nested  
403 polymerase chain reaction (PCR) in 25  $\mu\text{L}$  reactors filled up with 1  $\mu\text{L}$  of 5  $\mu\text{M}$  primer solution  
404 and 1  $\mu\text{L}$  of DNA matrix, diluted in a nucleotide-Taq polymerase-MgCl<sub>2</sub> mix. (Qiagen HoStar  
405 Taq master mix, Qiagen Inc., Valencia, CA). Reaction was performed in an ABI Veriti  
406 incubator (Applied Biosystems, Carlsbad, CA). Reaction products were reamplified by a  
407 second PCR step. Primers used in this second step were based on Illumina Nextera sequences:  
408 AATGATACGGCGACCACCGAGATCTACAC[i5index]TCGTCGGCAGCGT for the  
409 forward and -CAAGCAGAAGACGGCATAACGAGAT[i7index]GTCTCGTGGGCTCGG for  
410 the reverse. Generated amplicons were visualized with eGels (Life Technology, Grand Island,  
411 NY). Products were divided into several equimolar samples and sorted according to their size

412 by Agencourt AMPure XP (Beckman Coulter, Indianapolis, IN) on a 0.7 ratio basis for each  
413 step. DNA concentrations were determined with a Qubit 2.0 spectrofluorometer (Life  
414 Technologies, Grand Island, NY) and samples were then loaded in an Illumina MiSeq  
415 sequencing device (Illumina Inc., San Diego, CA), equipped with two fluid cells. The data have  
416 been deposited with links to BioProject accession number PRJNA492367.

417 Denoising, chimera checking, generation of operational taxonomic units (OTUs) and  
418 taxonomic classification were performed using the custom-scripted bioinformatics pipeline of  
419 the Research and Testing Laboratory (Lubbock, TX, USA). Based on the sequence identity  
420 percentage derived from BLASTn (Altschul et al., 1990), sequences with identity scores to  
421 known or well-characterized 16S rRNA gene sequences >97% identity (<3% divergence) were  
422 resolved at the species level, >95% to 97% at the genus level, >90% to 95% at the family level,  
423 >80% to 90% at the order level, >80 to 85% at the class level and between 77% – 80% at the  
424 phylum level. Any match below this identity level was not used in taxonomical analysis.  
425 Matrices of taxonomic data were further used to visualize changes in community composition.

426

### 427 *2.6.3. Bacterial diversity and composition analysis*

428 Principal Coordinate Analyses (PCoA) based on Bray-Curtis dissimilarities (Bray and  
429 Curtis, 1957; Odum, 1950) was used to visualize ecological gradients underlying the  
430 composition of bacterial communities of the environmental probes. PCoA were performed on  
431 R software with the *vegdist* function of the *vegan* package (Okasen *et al.*, 2016). The  
432 relationship between community profiles and the proportion of phylotypes in each sample was  
433 investigated by *a posteriori* projection of the genera as weighed average of their contribution  
434 to the samples onto the PCoA biplot. Discontinuities within the dataset were revealed by  
435 applying a Ward hierarchical clustering (Ward, 1963) as an aggregation rule on Bray-Curtis  
436 dissimilarities (Bray and Curtis, 1957; Odum, 1950) with the *hclust* function of the *stats*

437 package. Analysis of similarities (ANOSIM) was used to infer statistical differences between  
438 bacterial community clusters ( $P < 0.01$ ) whenever possible. Final clusters were selected on the  
439 basis of the corresponding average silhouette width. The significance of the axes in each biplot  
440 representation was evaluated following Kaiser-Guttman criterion.

441 To calculate the diversity and richness indices, the Illumina MiSeq sequences were re-  
442 analyzed using MOTHUR version 1.36.1 (<http://www.mothur.org>) starting from denoised and  
443 chimera-checked sequences, aligned, and clustered to define OTUs at 97% sequence identity.  
444 Two equivalent datasets were then randomly sub-sampled according to the procedure  
445 developed by Schloss *et al* (2009). The resulting datasets were used for rarefaction analysis and  
446 to calculate the diversity and richness indices (i.e., Shannon diversity index ( $H'$ ), inverse  
447 Simpson diversity and Chao 1 richness index ( $S_{chao1}$ ), Babcsanyi *et al.*, 2017).

448

### 449 **3. RESULTS**

#### 450 **3.1. Soil nutrient pool**

451 Soil physicochemical parameters are provided in Tables A.1-A.4. The profiles of Mg and  
452 Ca cationic exchange capacities as a function of depth, which corresponds to inorganic nutrients  
453 of interest in the present study, are shown in Fig. 2.

454

#### 455 **3.2. *In-situ* mineral dissolution rates**

456 Topography measurements on crystals incubated at the Strengbach catchment for 9 and 20  
457 months enabled to estimate the maximal dissolution rates based on surface retreats or roughness  
458 (Tables 1 and 2). The surface retreats for olivine ranged from 1 nm ( $9.38 \times 10^{-13}$  mol.m<sup>-2</sup>.s<sup>-1</sup>) to  
459 171 nm ( $7.17 \times 10^{-11}$  mol.m<sup>-2</sup>.s<sup>-1</sup>), both obtained from the meteoric sets of probes (at the weather  
460 station). Overall, upper boundaries of reaction rates for olivine were  $3.63 \times 10^{-11}$  mol.m<sup>-2</sup>.s<sup>-1</sup>

461 (meteoric),  $1.20 \times 10^{-11}$  mol.m<sup>-2</sup>.s<sup>-1</sup> (soil A horizon),  $1.12 \times 10^{-12}$  mol.m<sup>-2</sup>.s<sup>-1</sup> (soil C horizon) and  
462  $1.70 \times 10^{-12}$  mol.m<sup>-2</sup>.s<sup>-1</sup> (stream).

463 For labradorite, surface retreats ranged between 1 nm (stream, C horizon) and 5 nm  
464 (stream), corresponding to reaction rates ranging from  $1.92 \times 10^{-13}$  to  $2.15 \times 10^{-12}$  mol.m<sup>-2</sup>.s<sup>-1</sup>. The  
465 average upper boundaries of reaction rates for labradorite were  $6.21 \times 10^{-13}$  mol.m<sup>-2</sup>.s<sup>-1</sup>  
466 (meteoric),  $1.02 \times 10^{-12}$  mol.m<sup>-2</sup>.s<sup>-1</sup> (A horizon),  $6.20 \times 10^{-13}$  mol.m<sup>-2</sup>.s<sup>-1</sup> (C horizon) and  $1.37 \times 10^{-12}$   
467 mol.m<sup>-2</sup>.s<sup>-1</sup> (stream). Of note, Daval *et al.* (2018) indicated that the measured dissolution rates  
468 in the A horizon for labradorite powders incubated for over four years in the same location from  
469 2004 to 2008 ( $1.9 \times 10^{-12}$  mol.m<sup>-2</sup>.s<sup>-1</sup>) are similar to those reported above. For some samples, the  
470 surface retreat varied significantly along the boundary of the masks (Fig. 3). In such cases,  
471 zones with the greatest surface retreats may coincide with zones of preferential fluid circulation,  
472 as indicated by material fragments including colluvium or soil sediments (Fig. 3A and 3C  
473 (dashed area) and Fig. 4A and 4C (zone 2)). The surface retreats presented in Tables 1 and 2  
474 correspond to zones of maximal surface retreat on the crystals where fluid circulation could be  
475 evidenced, unless otherwise specified. In addition to global surface retreats (e.g. red arrow, Fig.  
476 5C), local dissolution features were detected (e.g. green arrow, Fig. 5C). These non-geometrical  
477 “etch pits” were generally randomly aligned and accounted for locally faster dissolution rates  
478 (see red color in Fig. 6B, D and E).

479

### 480 **3.3. Theoretical mineral reactivity**

481 Dissolution rates of olivine and labradorite in the soil profile were primarily controlled by  
482 seasonal temperature variations (for both A- and C-horizons, Fig. 7). Simulated pH values of  
483 the A horizon ( $4.3 \pm 0.2$ ) was in agreement with observed values ( $4.37 \pm 0.14$ ), whereas  
484 simulated values ( $5.4 \pm 0.2$ ) for the C horizon were slightly higher than those observed ( $4.83 \pm$   
485  $0.07$ ). The simulated solution compositions in the A and C horizons corresponded to far-from-

486 equilibrium conditions with respect to both labradorite and olivine (i.e.,  $\Omega$  values close to 0 in  
487 equation 5). Based on the transition state theory used in the WITCH model (equation 5), such  
488 undersaturation states corresponded to dissolution rates that were virtually not affected by the  
489 chemical affinity of the system.

490 For samples from the soil profile, predicted dissolution rates converted into global surface  
491 retreats were one to two orders of magnitude greater than rates measured *in-situ* for olivine  
492 (Table 2). The laboratory-field discrepancy for dissolution rates in the A horizon varied by a  
493 factor of 17 to more than 250 for olivine, and from about 7 to more than 50 for labradorite. In  
494 the C horizon, the minimum field-laboratory discrepancy was generally weaker, and ranged  
495 from 75 to more than 106 for olivine and from 2 to 7.5 for labradorite.

496 Regarding the set of probes exposed to the atmosphere, the predicted retreat based on the  
497 annual average rainfall properties (pH = 5.4; T = 7.1°C) overestimated the maximal measured  
498 retreats by a factor of about 2 for labradorite, and up to a factor of 80 for olivine. Of note, a  
499 sample of olivine locally exhibited a retreat of 171 nm, which corresponds to a factor of ~ 1 (no  
500 laboratory-field discrepancy).

501 For samples incubated in the Strengbach stream, theoretical calculations based on the  
502 annual average parameters describing water of the Strengbach stream (pH = 6.5; T = 5.8°C)  
503 overestimated the measured values by a factor of 9 to 19 for olivine, and a factor of  $\geq 1.8$  for  
504 labradorite.

505

### 506 **3.4. Diversification and composition of bacterial communities**

#### 507 *3.4.1. General patterns*

508 An average of 33,719 high-quality sequences (>~250 bp) were obtained for each sample by  
509 Illumina MiSeq after analysis with Mothur. The OTUs covered 29 phyla, 322 families and 722  
510 genera. Although the sequencing depth (see Fig. A.2 for rarefaction curves) did not

511 systematically allow for a survey of the full extent of bacterial diversity, rarefaction curves of  
512 diversity indices reached asymptotes (Fig. A.2). This indicates sufficient sampling depth to  
513 capture the diversity of bacterial communities.

514 Bacterial community composition of the soil, the weather station and the stream sets  
515 significantly differed ( $P < 0.01$ ), irrespective of the incubation time. Sets incubated at the  
516 weather station (Fig. 1G) were the richest in Cyanobacteria (> 18%) and in Bacteroidetes (>  
517 22%, Fig. 8), whereas those from the soil (Fig. 1C and D) were enriched in Acidobacteria  
518 (>20% horizon 1, > 16%, horizon B). Samples immersed in the stream (Fig. 1J) exhibited a  
519 higher mean abundance of Verrucomicrobia.

520 Differences between compartments of the CZ were also observed at the genus level, in  
521 particular amongst taxa potentially involved in mineral weathering processes. For instance,  
522 highest proportions of OTUs corresponding to *Geobacter* sp., typical from sedimentary  
523 environments and involved in Fe(III) reduction through anaerobic respiration (Esther *et al.*,  
524 2015), were found in the outlet samples. *Aquabacterium* sp. or *Rhodobacter* sp., which  
525 encompass several species known for their iron oxidizing capabilities (Hedrich *et al.*, 2011;  
526 Weber *et al.*, 2006), were only found in significant proportions in the stream set of probes.  
527 Genera known for their ability to weather iron-bearing silicates through siderophore production  
528 such as *Sphingomonas* sp. (Calvaruso *et al.*, 2007; Uroz *et al.*, 2009; Uroz *et al.*, 2007), or  
529 identified as dissimilatory iron-reducing bacteria (DIRB), such as *Acidiphilium* sp. (Esther *et*  
530 *al.*, 2015) were exclusively found in significant proportions on samples subjected to  
531 atmospheric weathering (i.e., at the weather station), especially on olivine samples. Both  
532 extracted DNA amounts and diversity indices were larger for the stream sets compared to the  
533 soil sets, and generally lower for the sets exposed to the atmosphere (Fig. A.3).

534 3.4.2. A- and C-horizons soil sets

535 Bacterial communities of the A horizon differed significantly from those of the C horizon  
536 ( $P < 0.01$ ). Taxa potentially involved in mineral alteration appeared to be unevenly distributed  
537 between A and C horizons. For example, phylotype sharing 100% similarity with  
538 *Mycobacterium kyorinense* strain KUM 060200 16S ribosomal RNA gene, belonging to the  
539 genus *Mycobacterium* associated to biotite alteration within the oak mycorrhizosphere (Uroz *et*  
540 *al.*, 2009), was only found in litter samples in relative abundance exceeding 0.1 %.

541 Clustering of samples from both the A and C horizons emphasized distinct communities for  
542 mineral probes or environmental matrices (i.e. soil) (Figs. 9 A and 9 C). In the A horizon,  
543 bacterial communities from the control empty bags incubated for 9 months, and the quartz  
544 samples incubated for 20 months, also differed from the rest of the samples (Fig. 9 D). These  
545 samples exhibited lower diversity than other samples from the A horizon, as evidenced by their  
546 inverse Simpson ( $I$ ) and Shannon ( $H'$ ) diversity indices (Fig. A.3 A and B). The richness and  
547 bacterial diversity of the olivine sample collected after 20 months of incubation in the A horizon  
548 (O20) were higher than for all other samples of the A horizon (Fig. A.3 A and B), and similar  
549 to richness and bacterial diversity of corresponding soil sample ( $S_{chaol} > 4000$ ; Fig. A.3 C).

550 Regarding the C-horizon, bacterial communities changed according to both incubation time  
551 (9-month samples *versus* 20-month samples, Fig. 9 A) and mineral type (Fig. 9 A). The bacterial  
552 diversity indices associated with labradorite and olivine were the highest ( $H' > 5$  and  $I > 50$ )  
553 after 20 months of incubation, and close to those of soil samples. Although diversity was on  
554 average lower after 9 months, bacterial diversity for labradorite and olivine was systematically  
555 larger than that for quartz. The bacterial diversity for labradorite was higher than that of olivine  
556 and quartz, although the bacterial richness for labradorite differed from that of other C horizon  
557 samples (Fig. A.3 C).

558 *3.4.3 Weather station*



559 Bacterial communities associated with mineral probes exposed to the atmosphere at the  
560 weather station were mainly structured according to the mineral type (Fig. 9 A and B). The  
561 average bacterial diversity was the lowest among the different sets of this study. The bacterial  
562 diversity was the highest for olivine and the lowest for quartz, and significantly increases for  
563 olivine between 9 months and 20 months. The olivine sample exhibited the largest specific  
564 richness after 20 months of incubation ( $S_{chaol} > 2000$ , Fig. A.3).

#### 565 3.4.4 Stream sets

566 Bacterial communities from samples immersed in the Strengbach stream differed from  
567 those of the related stream sediments (Fig. 9 G). The difference among mineral probes was  
568 lower compared to the difference between mineral probes and the stream sediments. Temporal  
569 changes in the bacterial communities were observed (Fig. 9 G). The bacterial diversity of  
570 environmental probes from the stream was greater than that of probes incubated in other  
571 compartments of the CZ ( $H' > 6.9$  and  $I > 400$ , Fig. A.3).

572

## 573 4. DISCUSSION

574 Dissolution rates of fresh mineral usually retrieved from laboratory experiments generally  
575 differ from rates of mineral aged in the field, due to changes in the mineral surface chemistry  
576 over geologic time scales. In addition, the biogeochemical weathering environment of minerals  
577 in the critical zone is still largely unknown. In this study, we incubated in the field mineral  
578 samples comparable to those used in laboratory experiments to identify *in-situ* (i) hotspots of  
579 mineral reactivity in the critical zone, (ii) the extent of the field-lab discrepancy, and (iii) main  
580 bacterial patterns associated to mineral surfaces. We discuss below the contribution of intrinsic  
581 and extrinsic factors to the field-laboratory discrepancy and factors that may be accounted for  
582 to limit this discrepancy. Possible effects of bacterial communities on mineral weathering and

583 the effect of extrinsic factors on mineralosphere development in contrasted compartment of the  
584 CZ are specifically addressed.

585

#### 586 **4.1. Contribution of intrinsic and extrinsic factors to the field-laboratory** 587 **discrepancy**

588 Field weathering rates of individual minerals are usually determined with indirect methods.  
589 In this study, nanoscale topography variations were used to directly probe mineral dissolution  
590 rates in the field (Figs. 5,6 and 10). A major finding is that up to two orders of magnitude  
591 separate field measurements and laboratory-based predictions (see Tables 1 and 2) from  
592 WITCH. Our *in-situ* measurements confirmed lower field weathering rates determined using  
593 indirect methods, although fresh surfaces (laboratory-type samples) were used here. The  
594 contribution of intrinsic and extrinsic factors to this discrepancy are discussed below.

##### 595 *4.1.1 Contribution of intrinsic surface aging*

596 Surface aging refers to any physicochemical modification of the surface of an altered  
597 silicate contributing to the decline of its dissolution rate. Surface aging has long been suggested  
598 to be an intrinsic factor that contributes to the field-lab discrepancy (Daval et al., 2017; Daval  
599 et al., 2018; Fischer et al., 2012; Gruber et al., 2014; Lüttge et al., 2013; Nugent et al., 1998;  
600 White and Brantley, 2003). We designed the present study to ensure that surface aging was  
601 unlikely to significantly affect dissolution rates of probed minerals.

602 Indeed, polished mineral surfaces used to probe *in-situ* dissolution rates of fresh silicate  
603 surfaces in the field minimized the contribution of intrinsic factors to the field-laboratory  
604 discrepancy. Assuming that aging (and the possible formation of passivation layers) requires a  
605 minimal portion of mineral surface to be weathered (in agreement with recent studies such as  
606 Gin et al. (2015) or Daval et al. (2018)), the reaction progress ( $\zeta$ ) after which it becomes  
607 significant (i.e., beyond the uncertainties of the measurement), should be specific to the

608 considered mineral at given conditions. Reaction progress ( $\xi$ ) quantifies here the extent of the  
609 reaction of dissolution (in  $\text{mol.m}^{-2}$ ) for either olivine or labradorite. In a recent study, Wild *et*  
610 *al.* (2016) reported that the decline of labradorite dissolution rate related to surface ageing was  
611 observed for  $\xi \geq 2.54 \times 10^{-3} \text{ mol.m}^{-2}$ . Regarding olivine, mineral ageing was evidenced in  
612 laboratory conditions for  $\xi \geq 6.92 \cdot 10^{-2} \text{ mol.m}^{-2}$  (Daval *et al.*, 2011). As reported in Tables 1 and  
613 2, the maximum reaction progress expected for labradorite and olivine, calculated as the product  
614 of the dissolution rate times the incubation period, reached  $\xi = 5.68 \cdot 10^{-4} \text{ mol.m}^{-2}$  (labradorite  
615 altered into the A horizon over 20 months) and  $\xi = 1.71 \cdot 10^{-2} \text{ mol.m}^{-2}$  (olivine altered into the A  
616 horizon over 20 months), respectively, which are below the threshold limit reported above.  
617 Hence, any difference between the measured and the modeled reaction rates can be attributed  
618 to extrinsic factors. In addition, fresh labradorite powders incubated in the A horizon of the  
619 exact same plot for durations exceeding four years were still far from being completely covered  
620 with passivating surface layers (Daval *et al.*, 2018), thereby further supporting this assertion.  
621 *In-situ* measurements could thus be directly compared with WITCH simulations that rely on  
622 kinetic rate laws obtained from laboratory experiments.

623

#### 624 4.1.2 Extrinsic factors in the laboratory-field discrepancy

625 Dissolution rates depend on extrinsic parameters, as emphasized in the simplified version  
626 of equation 5, adapted from (Lasaga, 1998):

$$R_{min} = A \cdot \exp\left(\frac{-E_{a,min}^i}{RT}\right) \cdot a_{H^+}^n \cdot f(\Delta G_{r,sil}), \quad (9)$$

627 describing mineral weathering rate  $R_{min}$  as a function of temperature  $T$ , the Gibbs free energy  
628 with respect to silicate (*sil*) dissolution  $\Delta G_{r,sil}$ , and the pH of the fluid, quantified by the  
629 chemical activity of protons ( $a_{H^+}^n$ ). These three parameters are the main extrinsic factors that  
630 control the aqueous mineral dissolution rate. Aside from the gas constant  $R$ , the other  
631 parameters of this equation, such as the Arrhenius pre-exponential factor  $A$ , the activation

632 energy  $E_{a,min}^i$ , and the reaction order  $n$  are constants derived from laboratory experiments,  
633 which are specific to the considered dissolution reaction.

634 A wide range of values has been reported for each of these three parameters, even for the  
635 same mineral (Palandri and Kharaka, 2004). Such disparities in parameter values can lead to  
636 significant uncertainties between predicted mineral dissolution rates (Rimstidt *et al.*, 2012).  
637 Parameters chosen for the present study were retrieved from Rosso and Rimstidt (2000) data  
638 for olivine ( $A = 3.467 \text{ mol.m}^{-2}.\text{s}^{-1}$ ,  $E_a = 42.6 \text{ kJ.mol}^{-1}$ , and  $n = 0.50$ ) and Palandri and Kharaka  
639 (2004) data for labradorite ( $A = 0.321 \text{ mol.m}^{-2}.\text{s}^{-1}$ ,  $E_a = 42.1 \text{ kJ.mol}^{-1}$ , and  $n = 0.63$ ). These two  
640 studies provide a meta-analysis of experimental kinetic data and apply statistical methods to  
641 infer the rate parameters reported above. We verified that the corresponding rate laws  
642 satisfactorily predict dissolution rates of the labradorite and olivine powders reacted in mixed  
643 flow set-ups, using the soil solutions collected from lysimetric plates at the Strengbach  
644 catchment (see details in Wild *et al.* (2018)).

645 As temperature is an input parameter of the numerical simulations, it can be ruled out as a  
646 factor explaining the field-laboratory discrepancy. Since simulated pH values were either  
647 similar to those measured, or slightly higher, the contribution of this parameter to the minimal  
648 field-lab discrepancy reported in Tables 1 and 2 is negligible. Hence, the observed field-  
649 laboratory discrepancy can be ascribed either to the effect of  $\Delta G_{r,sil}$  quantified by the  $f(\Delta G_{r,sil})$   
650 function, or to the fluid-mineral contact time, which is an implicit condition to equation 9.

651 Surface retreats could only be distinguished in areas where fluid circulation occurred on  
652 labradorite and olivine samples (see section 3.2 and Figs. 3 and 4, respectively). This indicates  
653 that the temporal and spatial extents of fluid-mineral contact may partly account for the field-  
654 laboratory discrepancy. In terms of spatial extent of the fluid-mineral interface, no compact  
655 coating of secondary minerals potentially masking significant portion of mineral surface could  
656 be observed on mineral surfaces after incubation. This hypothesis was therefore ruled out.

657 The extent of fluid-mineral contact time parameter is, on the other hand, indirectly  
658 implemented in WITCH with the soil moisture saturation factor (*SMS*) given in equation 4.  
659 *SMS* estimates the proportion of the bulk soil volume saturated with aqueous solution for a  
660 given depth, which corresponds to the proportion of minerals that is susceptible to exchange  
661 matter with the fluid. However, the *SMS* does not allow to localize fluid circulation zones at  
662 the soil profile scale. The discrepancy between the data and the model (Fig. 11) is unlikely to  
663 result from the hydrological budget alone since the concentration of conservative tracers, such  
664 as sulfate anions, fitted observation for the A-horizon (see section 2.5 and Table A.5). Indeed,  
665 surface retreats measured for mineral probes of the stream sets were at best one order of  
666 magnitude lower than those estimated with kinetic rate laws derived from laboratory  
667 experiments, despite permanent fluid-mineral contact (Tables 1 and 2).

668 Finally, the effect of the Gibbs free energy of reaction on mineral dissolution rate may  
669 contribute to explain the field-lab discrepancy. The dependence of mineral dissolution rate on  
670  $\Delta G_{r,sil}$  is implemented in WITCH through the  $(1 - \Omega)$  term in equation 5, in agreement with  
671 the transition state theory (TST), which is equivalent to:

$$f_1(\Delta G_r) = 1 - \left[ \exp\left(\frac{\Delta G_r}{RT}\right) \right]^s \quad (10)$$

672 in equation (9). Even though this relation is widely used in reactive transport codes and  
673 sometimes successfully applied to reproduce field observations (Godd ris and Donnadi u,  
674 2009; Godderis et al., 2006; Violette et al., 2010), it may not be appropriate to describe complex  
675 reaction pathways (Gin *et al.*, 2008). For instance, the sum of two parallel reactions, with a  
676 transition from far-to-equilibrium to close-to-equilibrium dissolution regime occurring at  $\Delta G_r$   
677  $= -7.5 \text{ kcal.mol}^{-1}$ , better described the dissolution kinetics of labradorite (Taylor *et al.*, 2000).  
678 To test the effect of the selection of the  $f(\Delta G_{r,sil})$  function, the empirical relation of Taylor *et*  
679 *al.* (2000) was implemented in WITCH:

$$f_2(\Delta G_r) = \left\{ \begin{array}{l} 0.76 * \left[ 1 - \exp \left( -1.3 * 10^{-17} * \left( \frac{|\Delta G_r|}{RT} \right)^{14} \right) \right] \\ + 0.24 * \left[ 1 - \exp \left( -0.35 * \frac{|\Delta G_r|}{RT} \right) \right] \end{array} \right\} \quad (11)$$

680 with the exception of a minor sign correction (the original paper mistakenly indicates -0.24  
681 instead of +0.24 for eq. 11). Variations of the  $f_1$  and  $f_2$  functions for the A and C horizons are  
682 shown in Fig. 11 A.  $\Delta G_{r,sil}$  did not affect labradorite dissolution rate in the soil profile if one  
683 considers the  $f_1$  function. In contrast, a significant decrease of the apparent dissolution rate of  
684 labradorite in the C horizon occurred using the  $f_2$  function. Regarding the C horizon, changing  
685 the  $f(\Delta G_{r,sil})$  function for the  $f_2$  function totally resolved the field-laboratory discrepancy for  
686 labradorite, as shown by values of  $\Delta_{L/F} < 1$  (parenthesis, Table 1) and in agreement with Gruber  
687 *et al.*, 2014. For the A-horizon, however, the field-laboratory discrepancy could not be totally  
688 explained by the equilibrium term since the discrepancy persisted ( $\Delta_{L/F} > 1$ ). Regarding olivine,  
689 in the absence of an alternative function describing the  $R_{min} - \Delta G_{r,sil}$  dependence of its  
690 dissolution kinetics, the TST-based relation was used by default, although it may not be fully  
691 relevant.

692 Overall, this shows that current models may partly fail to capture the effects of both  
693 heterogeneity of fluid circulations and local physicochemical conditions on mineral dissolution  
694 rates in soils of the CZ. The presence of microorganisms associated to minerals may be one of  
695 the factors influencing both fluid circulation and local physicochemical conditions. The  
696 relationship between bacterial communities and minerals in various compartments of the CZ is  
697 discussed below.

698

#### 699 **4.2. Effect of microorganisms on mineral weathering in the CZ**

700 Amongst other extrinsic parameters, biota has been shown to affect mineral weathering  
701 (Ahmed and Holmstrom, 2015; Bonneville *et al.*, 2009; Courty *et al.*, 2010; Li *et al.*, 2016;

702 Uroz *et al.*, 2009). Most strikingly, the weathering rate for the olivine surface incubated for 9  
703 months at the weather station were low, corresponding to a retreat < 1 nm (Table 2), whereas  
704 the surface incubated for 20 months exhibited an exceptional retreat of up to 172 nm (Fig. 10),  
705 corresponding to a field-laboratory discrepancy value of  $\Delta_{L/F} = 1$  (no discrepancy, see Table  
706 2). Rainwater cannot be considered as the unique weathering agent for olivine because open-  
707 air incubation conditions offer rather homogeneous input weathering conditions. Variations of  
708 reaction rates are at odds with the exposure of olivine surface to homogeneous reactive fluids  
709 at the weather station. In addition, the mineral surface retreat measured after 20 months would  
710 virtually corresponds to a permanent interaction of the mineral with a fluid of average  
711 composition of the rainwater. This condition is unlikely as the samples incubated at the weather  
712 stations were prone to drying-wetting cycles. In addition, permanent fluid interaction is  
713 inconsistent with the retreat observed after 9 months of incubation in the same conditions  
714 (sample MO9, Table 2). The occurrence of several microorganisms on the meteoric probes  
715 supports the hypothesis that organisms contributed to mineral weathering.

716 Microorganisms can also affect locally fluid circulation in soil (Or *et al.*, 2007), which can  
717 impact mineral weathering by regulating fluid-mineral contact. More specifically, biofilms can  
718 disrupt interactions between mineral surface and bulk fluid and stabilize locally zones of  
719 preferential fluid circulation. Here, samples from the A-horizon show that the flow path of the  
720 solution can be precisely constrained around the fluid boundary ( $\pm 10 \mu\text{m}$ , approximate width  
721 of the transition zone indicated by dashed lines in Fig. 4G) (Fig. 4D-F). Biofilms may thus  
722 subtly control fluid flow and act similarly to the RTV glue used to estimate global surface retreat  
723 (dark grey area, Fig. 4C and striped area, Fig. 4D-F and 4H).

724 While biofilm may have increased the dissolution rate of olivine exposed to meteoric fluid  
725 or indirectly contributed to the field-lab discrepancy by affecting fluid-mineral contact, direct  
726 observation of mineral-microorganism contact is missing to support such hypothesis.

727 Concerning soil compartments, no clear direct evidence of bacterial weathering could be  
728 observed despite biological weathering could have been favored by K, Ca and Mg  
729 concentrations typical for nutrient-poor pedological systems (van der Heijden *et al.*, 2013). Mg  
730 concentrations in the soil profile (Fig. 2) were similar to those observed in a reference forest  
731 plot located in the Morvan Mountains (Burgundy, France), which exhibited Mg-deficiency  
732 thirty years after clear-cutting native forest (van der Heijden *et al.*, 2013). Moreover, symptoms  
733 of forest decline, and Mg and Ca nutritional deficits in trees were already described at the  
734 Strengbach catchment (Dambrine *et al.*, 1992). We thus tried to indirectly probe clues possible  
735 mineral-bacteria interactions by tracking the development of mineral-specific bacterial  
736 communities, and how their composition varied according to the mineral substrates (Jones and  
737 Bennett, 2014) or their dissolution rates (Uroz *et al.*, 2012). The influence of minerals on  
738 bacterial communities in their direct vicinity and the potential for mineral weathering of  
739 bacterial phylotypes found in the environmental probe are discussed below. However, one has  
740 to keep in mind that only about 6% of the bacterial phyla are identified by usual taxonomic  
741 databases (Solden *et al.*, 2016; Yarza *et al.*, 2014). Therefore, relating weathering fluxes to  
742 specific bioweathering bacteria in the field solely based on their phylogenetic affiliation  
743 remains an elusive goal. In this exploratory study, the relevance of bacterial diversity as a  
744 potential indicator of the mineral-bacteria interactions was evaluated.

745

#### 746 *4.2.1 Establishment of mineral-specific bacterial communities*

747 Our results are consistent with the hypothesis that incubated minerals host specific  
748 mineralosphere bacterial communities. Indeed, mineralosphere bacterial communities from the  
749 soil profile or the Strengbach stream differed from those of the corresponding bulk soil or  
750 stream sediment samples respectively. Similarly, mineral-specific communities from the  
751 meteoric sets established according to the mineral type. This is in agreement with previous



752 results obtained with a similar approach using *in-situ* incubation of fresh minerals (Mitchell *et*  
753 *al.*, 2013; Uroz *et al.*, 2012), field samples (Gleeson *et al.*, 2006), or microcosms inoculated  
754 with microbial consortia from a forest soil (Heckman *et al.*, 2013). This point is highlighted  
755 here since the development of mineral-specific bacterial communities may reflect the  
756 development of phylotypes adapted to mineral weathering, along with the development of  
757 bioweathering processes adapted to the mineral substrate.

758         Interestingly, our results also show that mineralosphere communities changed over time.  
759 While previous studies provided “snapshots” of mineralosphere bacterial communities  
760 (Mitchell *et al.*, 2013; Uroz *et al.*, 2012), two incubation times were considered in the present  
761 approach (9 and 20 months), which constitutes an attempt to address temporal changes of  
762 bacterial communities. In the C soil horizon and stream sets of probes, time rather than intrinsic  
763 mineral weatherability seemed to constitute a primary factor driving community composition  
764 (Fig. 9 E). In probes from the C horizon, bacterial communities associated with olivine and  
765 labradorite differed more from those associated with non-reactive samples (quartz) after 20  
766 months of incubation than in the initial stages of the mineralosphere formation (i.e., after 9  
767 months). This support the idea that the mineralosphere develops according to mineral reactivity  
768 under field conditions, even though more probes and replicates in each CZ compartments are  
769 necessary to confirm this trend.

770

#### 771                   4.2.2. *Influence of extrinsic factors on mineralosphere development*

772         Comparison of environmental probes incubated in the atmospheric, soil and stream  
773 compartments of the CZ revealed the effect of extrinsic factors (i.e., not related to the mineral)  
774 on mineralosphere bacterial communities. Altogether, the results suggest that the relative  
775 contribution of extrinsic *versus* intrinsic factors on the differentiation of bacterial communities

776 increases across CZ compartments, following a meteoric < C-horizon < A-horizon < stream  
777 pattern.

778 The meteoric sets of probes were exclusively exposed to atmospheric inputs, which are  
779 intermittent and nutrient-poor compared to those recorded in the soil or in the stream. In soils,  
780 the hygrometry and cationic inputs may be buffered by secondary mineral phases. By contrast,  
781 the composition of the fluid in direct contact with mineral probes in the stream was rapidly  
782 controlled by the stream hydrochemistry. In the case of the meteoric sets of probes, the mineral  
783 type was expected to largely control the surface environment, and thus the response of bacterial  
784 communities. Indeed, the mineral represented the main source of inorganic nutrients and/or  
785 toxic elements, such as Al (Jones and Bennett, 2014; Singh et al., 2005). Lower overall bacterial  
786 diversity for the meteoric sets of probes compared to other sets, and distinct bacterial  
787 communities (Fig. 9 A) and diversity (Fig. A.3) according to the mineral substrate, support this  
788 hypothesis. The lower impact of external inputs in the case of meteoric probes may also explain  
789 the rapid differentiation of bacterial communities according to the mineral type, regardless of  
790 the incubation time.

791 Contrasting with observations from the C horizon and meteoric sets of probes, bacterial  
792 communities from the A horizon did not cluster according to mineral type. This may reflect  
793 more dynamic conditions in the A horizon with respect to both physicochemical conditions and  
794 microbial diversity. This is suggested by heterogeneous flows that were evidenced on the probe  
795 surface (Fig. 3 and Fig. 4). In addition, organic matter cycling and bioturbation (Gutiérrez and  
796 Jones, 2006) may particularly affect, on the short-term, microorganisms of the A horizon by  
797 altering nutrient inputs or physicochemical parameters. This may tremendously confound and  
798 delay the response of microbial communities to mineral reactivity.

799 The effect of extrinsic factors was apparently even stronger in the case of the stream probes  
800 because fluid circulation directly and continuously impacted the physicochemical

801 characteristics of the incubation environment (T, pH, etc.). This is emphasized by the similar  
802 composition of bacterial communities observed amongst samples in the stream set of probes  
803 (Fig. 9 H) and the higher bacterial diversity observed on these samples compared to other  
804 compartments (Fig. A.3). In this case, continuous inputs of dissolved nutrients and particle-  
805 associated biomass (Fig. 1 J) may interfere with the development of the mineralosphere. This  
806 may in turn challenge and delay the detection of a mineralosphere effect (i.e., specific bacterial  
807 communities associated to specific minerals). Analogous effects were observed in an oceanic  
808 context, where minerals incubated close to hydrothermal discharge (providing a continuous  
809 input of nutrient from fluids) only served as a solid support on which bacteria could attach,  
810 whereas similar minerals located far from these fluids inputs served as Fe source for  
811 microorganisms (Henri et al., 2016). As a result, the effect of extrinsic factors on the  
812 differentiation of mineralosphere bacterial communities may largely differ among CZ  
813 compartments for similar incubation times.

814

#### 815 *4.2.3. Occurrence of potential mineral-weathering bacteria*

816 Potential mineral-weathering bacterial taxa found in the environmental probes included  
817 *Pseudomonas* sp., *Collimonas* sp., *Burkholderia* sp., *Janthinobacterium* sp., *Leifsonia* sp., and  
818 *Arthrobacter* sp. The occurrence of these taxa underscores the potential for biotic alteration in  
819 the mineralospheres of the investigated soils. These taxa were found in higher abundance not  
820 only in the sets of probes incubated in the soil profile compared to other compartments (2.1%  
821 vs. 0.1% on average, Fig. 12), but also in the mineralosphere compared to the corresponding  
822 bulk soil horizons (2.6% vs. 0.2% on average, Fig. 12).

823 *Pseudomonas* sp. dominated the studied mineralospheres, with an average proportion of  
824 2.5% for the whole dataset and of 4.5% in the soil samples (< 0.1% for the other compartments  
825 of the critical zone). Phylotypes belonging to the *Pseudomonas* genus have been described in

826 the literature for their ability to dissolve biotite (Uroz *et al.*, 2009). For both the A and C  
827 horizons of the soil profile, *Pseudomonas* sp. was more abundant on labradorite and olivine  
828 samples. The proportion of *Pseudomonas* sp. remained constant over time in samples from the  
829 C horizon, whereas it decreased in the A horizon between 9 and 20 months of incubation (Fig.  
830 12). This suggests that *Pseudomonas* sp. pioneered the colonization of the mineral probes of  
831 the soil sets, and mainly occurred in relation to saprolitic alteration. This may be due to the  
832 significance of rock weathering in the C horizon relative to other processes that may affect  
833 microbial assemblages in the A horizon (e.g. bioturbation, degradation of organic matter or  
834 nutrient cycling).

835 *Collimonas* sp. was also particularly abundant in the soil mineral probes (1.9%) compared  
836 to other compartments (< 0.1%). It has long been thought that species belonging to the  
837 *Collimonas* genus were bacteria living at the expense of organic exudates produced by fungi of  
838 the mycorrhizosphere (de Boer *et al.*, 2004). However, *Collimonas* sp. are also capable of  
839 extracting elements, such as iron from biotite (Calvaruso *et al.*, 2007; Uroz *et al.*, 2007), or  
840 from granite powders (Lapanje *et al.*, 2012) by the production of siderophores, thus supplying  
841 their fungal hosts with inorganic nutrients. In our samples, *Collimonas* sp. was found in a larger  
842 proportion in the C horizon (i.e., in contact with the saprolite) than in the organic-rich A  
843 horizon.

844 The projection of *Collimonas* sp. found for each of the corresponding PCoA analyses (Fig.  
845 9) revealed similar trends for samples from the two soil horizons. *Collimonas* sp. prevailed on  
846 quartz and labradorite after 9 months of incubation, whereas it decreases in all samples between  
847 9 and 20 months, except for olivine, where it increases over the same period. The decline of  
848 *Collimonas* sp. was associated to increasing bacterial diversity in all sets of probes incubated  
849 in the soil, except for quartz in the A horizon (Fig. A.3). This suggests that *Collimonas* sp. may

850 first establish at the fungus-rock interface, before specializing in iron extraction through the  
851 production of siderophores.

852 In average, *Burkholderia* sp. accounted for 1.0% of the total genera recovered from the  
853 probes. *Burkholderia* sp. have been reported to enhance the dissolution of biotite, like some  
854 members of the genus *Collimonas* (Calvaruso *et al.*, 2007; Uroz *et al.*, 2007), but also apatite  
855 (Lepleux *et al.*, 2012; Mailloux *et al.*, 2009), phosphate minerals (Kim *et al.*, 2005; Vassilev *et*  
856 *al.*, 2006), quartz (Ullman *et al.*, 1996), bytownite (Barker *et al.*, 1998; Welch *et al.*, 1999) and  
857 other feldspars (Ullman *et al.*, 1996), and more generally granite (Wu *et al.*, 2008) or basalt  
858 (Wu *et al.*, 2007). Similarly to *Collimonas* sp., *Burkholderia* sp. was mainly found in soil  
859 compartments, especially in the A horizon, in particular associated to the quartz sample  
860 incubated for 20 months. The latter sample also exhibits a notably low bacterial diversity ( $H' < 5$   
861 and  $I < 50$ , Fig. A.3). *Burkholderia* sp. therefore seems to correspond to "lithophilic" bacteria  
862 particularly adapted to the context of the A horizon.

863 *Janthinobacterium* sp., *Leifsonia* sp. and *Arthrobacter* sp., which have been described for  
864 their ability to dissolve granite through the production of oxalic acid and hydrogen cyanide  
865 (Frey *et al.*, 2010), also belonged to the first decile of most abundant bacterial genera. Biotite  
866 dissolution was enhanced by species of the genus *Janthinobacterium* (Uroz *et al.*, 2009).  
867 Species belonging to the genus *Arthrobacter* may promote the dissolution of hornblende  
868 (Kalinowski *et al.*, 2000), quartz and feldspars (Ullman *et al.*, 1996), including bytownite  
869 (Barker *et al.*, 1998; Welch *et al.*, 1999). The proportions of *Leifsonia* sp. and *Arthrobacter* sp.  
870 after 9 months was higher in the C horizon compared to the A horizon, whereas the proportions  
871 were larger in quartz samples after 20 months in both soil horizons (Fig. 12). *Leifsonia* sp., or  
872 *Arthrobacter* sp. may preferentially adapt to environments with a lower influence of extrinsic  
873 factors, like in the C horizon compared to the A horizon (see section 4.2.2 and Fig. 12), or to  
874 the quartz surface, not releasing any toxic or valuable elements. This results in high apparent

875 proportion for the samples associated to low diversity, such as the quartz samples.  
876 *Janthinobacterium* sp. occurred in a larger proportion in probes from the C horizon, in particular  
877 on olivine and labradorite probes that bear elements of interest such as Mg, Fe or Ca (Fig. 12).  
878 The population decrease between 9 and 20 months of incubation suggests that  
879 *Janthinobacterium* sp. may be "lithophilic" and compete with other bacterial processes, as  
880 described above.

881 Finally, *Polaromonas* sp., which was previously reported in the context of granite  
882 weathering (Frey *et al.*, 2010), was present in high proportions in all sets of probes of the C  
883 horizon.

884 Overall, bacterial communities of mineralosphere of the soil profile feature several  
885 populations that may be involved in mineral weathering. The distribution of bacterial taxa  
886 putatively associated with mineral weathering coincided with the disturbed bacterial pattern of  
887 the A horizon. Indeed, extrinsic factors (i.e. factors influencing the bacterial community that  
888 are not related to the mineral substrate) may considerably affect the distribution of the taxa  
889 potential associated with mineral weathering, such as *Pseudomonas* sp., *Janthinobacterium* sp.,  
890 *Leifsonia* sp., or *Arthrobacter* sp. Such disturbances may delay the development of a  
891 mineralosphere specific to the mineral type.

892

#### 893 *4.2.4 Do bacteria with weathering ability actively dissolve minerals?*

894 Determining whether microorganisms with known weathering activity and present at the  
895 surface of minerals actively contribute to mineral dissolution remains challenging. While to  
896 date most of the evidences of bacterial mineral dissolution have been based on microscopic  
897 observations (Bennett *et al.*, 2001; Jongmans *et al.*, 1997), this approach is still controversial  
898 (Benzerara *et al.*, 2007). Another methodology has been suggested, which considers a linear  
899 relationship between *in-situ* weathering rates and bacterial diversity (Uroz *et al.*, 2012). In our

900 case, however, no clear correlation could be established between the extent of mineral  
901 weathering and bacterial diversity or enrichment of specific taxa (i.e., *Collimonas* sp.,  
902 *Burkholderia* sp., *Pseudomonas* sp., *Janthinobacterium* sp., *Leifsonia* sp., or *Arthrobacter* sp.).  
903 However, these specific taxa, which may be functionally related to mineral weathering, do not  
904 necessarily express this function, and their occurrence may not necessarily reflect a selective  
905 pressure for their bioweathering ability.

906       Nevertheless, regarding samples exposed to open-air weathering at the weather station,  
907 bacterial diversity globally increases with increasing mineral weatherability (quartz <  
908 labradorite < olivine), irrespective of the mineral incubation time. This supports the clustering  
909 of bacterial communities according to the mineral substrate shown in Fig. 9 A. In the A-horizon,  
910 the Shannon and inverse Simpson diversity indices are higher for olivine (the most weatherable  
911 mineral) incubated 20 months in the A horizon than for all the other mineral samples of this  
912 compartment (Fig. A.3). The potential for nutrient mobilization of a given mineral may thus  
913 stimulate competition between bioweathering agents and support the development of diverse  
914 bacterial communities.

915       Regarding the C horizon, variation in the diversity indices echoes the cluster analysis (Fig.  
916 9 E). This stresses the first-order importance of time on the composition of bacterial  
917 communities: time prevailed over the type of the mineral in the C horizon. Globally, diversity  
918 increased for all three minerals as a function of time. On the other hand, diversity was  
919 significantly higher for "reactive" minerals after 20 months of incubation and reached that of  
920 the corresponding soil samples (Fig. A.3 A, B). Bacterial richness (Chao 1 index) was only  
921 significantly higher for labradorite after 20 months, which reflected the diversification of  
922 bacterial communities in the C horizon for minerals. The low differences of bacterial diversity  
923 between mineral samples immersed in the Strengbach stream confirms the second-order role  
924 played by mineral substrates for this compartment.

925 To conclude, diversity analysis of bacterial communities for samples incubated in the A  
926 and C horizons of the soil profile and at the weather station suggests a relationship between  
927 microbial community diversity and mineral reactivity. Our results support the hypothesis that  
928 mineral substrates, depending on their incubation context, may affect microbial communities  
929 in their mineralospheres. Diversity analysis of bacterial communities suggests that potential  
930 bioweathering bacteria of the A horizon are preferentially associated to (Mg, Fe)-bearing  
931 phases, such as olivine, whereas those of the C horizon are rather associated to feldspars  
932 minerals, such as labradorite. However, this study is not fully conclusive as to whether the  
933 potential of bacterial weathering is actually expressed. This would require strengthening the  
934 statistical significance of the results by increasing the number of probes and replicates on the  
935 one hand, and to statistically relate dissolution features to bioweathering processes. To address  
936 this issue, future studies may consider imaging spatial distribution of microorganisms on  
937 mineral samples, especially by assessing their distance from the surface or from dissolution  
938 “hot spots” with confocal laser scanning microscopy. Once microorganisms are located on the  
939 mineral surface, possible associated dissolution features of biotic origin may be used to quantify  
940 associated “biotic rates” by rate spectra analysis (Fischer et al., 2012), such as that presented  
941 on Fig. 6.

942

## 943 **5. SUMMARY AND CONCLUSIONS**

944 The present study shows that *in-situ* mineral dissolution rates and bioweathering  
945 environments of minerals can be directly probed *in-situ* in contrasted compartments of the CZ.  
946 This approach is complementary to those already used to estimate mineral weathering rates in  
947 the field, as it allows for the estimation of mineral weathering rates over short timescales (from  
948 months to years).



949 In spite of the limited number of samples that could be incubated, fundamental parameters  
950 to understand mineral dissolution in the CZ were identified. In particular, extrinsic factors may  
951 partly explain the gap existing between estimates of silicate dissolution rates obtained in the  
952 laboratory and in the field, while potential bioweathering bacteria were found in all CZ  
953 compartments. Salient results of the present study can be summarized as follows:

954 1) In A and C soil horizons, simulated dissolution rates converted into global surface  
955 retreats were greater by a factor of 1 to 270 for olivine, and of 2 to 54 for labradorite  
956 than those measured *in-situ*.

957 2) The heterogeneity of fluid circulation in soil profiles should be accounted for in  
958 chemical weathering models as it can significantly affect *in-situ* mineral weathering  
959 rates.

960 3) The effect of the Gibbs free energy of reaction on labradorite dissolution rates partly  
961 explains the discrepancy between laboratory estimates and field measurements for the  
962 A and C soil horizons.

963 4) The nature of the mineral substrate affects bacterial communities of the mineralosphere.  
964 This process can however be affected or delayed by extrinsic factors, such as nutrient  
965 or biomass inputs mediated by fluid circulation.

966

967 In parallel, our study also raised some issues that need to be explored in the future. Although  
968 potential bioweathering bacterial phylotypes were detected on environmental probes incubated  
969 in A and C horizons, bioweathering activities could not be proved, and the contribution of  
970 bacterial activities to the total weathering flux could not be quantified. The approach proposed  
971 in this study may however be generalized to evaluate *in-situ* expression of microbial  
972 bioweathering functions (i) to quantify the effect of microbial communities on mineral

973 dissolution rate, and (ii) to gradually include bacteria/mineral interactions in next-generation  
974 chemical weathering models.

975 Finally, incubation of a greater number of integrative reactivity probes of various mineral  
976 types may help in the future to unravel effective local reaction conditions controlling *in-situ*  
977 mineral reactivity in CZ compartments.

978

## 979 **6. ACKNOWLEDGEMENT**

980 The making of probes and of the experimental setup benefited from the technical support of  
981 Lisa Wild and René Wild that are warmly acknowledged. The follow up of the experiment  
982 would have not been possible without the help of the OHGE team, and particularly Solenn Cotel  
983 and Sylvain Benarioumlil. Authors also wish to thank Michael Heap, Heline Maison and Gilles  
984 Morvan for technical assistance and François Guyot for numerous and fruitful discussions that  
985 contributed to this manuscript. This work was funded through a grant to Gwenaël Imfeld for  
986 the project MicXtreme under the framework of the LabEx G-EAU-THERMIE PROFONDE  
987 project ANR-11-LABX-0050, and through a grant to Damien Daval under the framework of  
988 the VALVE project (EC2CO-BIOHEFECT program coordinated by the CNRS–Institut  
989 National des Sciences de l’Univers).

990

991

992

993

994

## 995 **7. REFERENCES CITED**

996

997 Ackerer, J., Chabaux, F., Van der Woerd, J., Viville, D., Pelt, E., Kali, E., Lerouge, C.,  
998 Ackerer, P., Roupert, R.D., Negrel, P., 2016. Regolith evolution on the millennial timescale  
999 from combined U-Th-Ra isotopes and in situ cosmogenic Be-10 analysis in a weathering profile  
1000 (Strengbach catchment, France). *Earth Planet. Sci. Lett.* 453, 33-43.

1001 Ahmed, E., Holmstrom, S.J.M., 2015. Microbe-mineral interactions: The impact of surface  
1002 attachment on mineral weathering and element selectivity by microorganisms. *Chem. Geol.*  
1003 403, 13-23.

1004 Alisa Mast, M., Drever, J.I., 1987. The effect of oxalate on the dissolution rates of oligoclase  
1005 and tremolite. *Geochim. Cosmochim. Acta* 51, 2559-2568.

1006 Altschul, S.F., Gish, W., Miller, W., Myers, E.W., Lipman, D.J., 1990. Basic local  
1007 alignment search tool. *J. Mol. Biol.* 215, 403-410.

1008 Alveteg, M., 1998. Dynamics of forest soil chemistry. Ph.D, Lund University.

1009 Arvidson, R.S., Ertan, I.E., Amonette, J.E., Luttge, A., 2003. Variation in calcite dissolution  
1010 rates: A fundamental problem? *Geochim. Cosmochim. Acta* 67, 1623-1634.

1011 Arvidson, R.S., Luttge, A., 2010. Mineral dissolution kinetics as a function of distance from  
1012 equilibrium - New experimental results. *Chem. Geol.* 269, 79-88.

1013 Augusto, L., Turpault, M.P., Ranger, J., 2000. Impact of forest tree species on feldspar  
1014 weathering rates. *Geoderma* 96, 215-237.

1015 Babcsanyi, I., Meite, F., Imfeld, G., 2017. Biogeochemical gradients and microbial  
1016 communities in Winogradsky columns established with polluted wetland sediments. *FEMS*  
1017 *Microbiol. Ecol.* 93.

1018 Barker, W.W., Banfield, J.F., 1996. Biologically versus inorganically mediated weathering  
1019 reactions: Relationships between minerals and extracellular microbial polymers in lithobiotic  
1020 communities. *Chem. Geol.* 132, 55-69.

1021 Barker, W.W., Welch, S.A., Chu, S., Banfield, J.F., 1998. Experimental observations of the  
1022 effects of bacteria on aluminosilicate weathering. *Am. Miner.* 83, 1551-1563.

1023 Beaulieu, E., Godderis, Y., Donnadieu, Y., Labat, D., Roelandt, C., 2012. High sensitivity  
1024 of the continental-weathering carbon dioxide sink to future climate change. *Nat. Clim. Change.*  
1025 2, 346-349.

1026 Beaulieu, E., Godderis, Y., Labat, D., Roelandt, C., Oliva, P., Guerrero, B., 2010. Impact  
1027 of atmospheric CO<sub>2</sub> levels on continental silicate weathering. *Geochim. Cosmochim. Acta* 74,  
1028 A65-A65.

1029 Beig, M.S., Luttge, A., 2006. Albite dissolution kinetics as a function of distance from  
1030 equilibrium: Implications for natural feldspar weathering. *Geochim. Cosmochim. Acta* 70,  
1031 1402-1420.

1032 Bennett, P.C., Hiebert, F.K., Choi, W.J., 1996. Microbial colonization and weathering of  
1033 silicates in a petroleum-contaminated groundwater. *Chem. Geol.* 132, 45-53.

1034 Bennett, P.C., Rogers, J.R., Choi, W.J., 2001. Silicates, silicate weathering, and *Microb.*  
1035 *Ecol.* *Geomicrobiol. J.* 18, 3-19.

1036 Benzerara, K., Menguy, N., Banerjee, N.R., Tyliszczak, T., Brown, G.E., Guyot, F., 2007.  
1037 Alteration of submarine basaltic glass from the Ontong Java Plateau: A STXM and TEM study.  
1038 *Earth Planet. Sci. Lett.* 260, 187-200.

1039 Bonneau, M., Dambrine, E., Nys, C., Range, r.J., 1991. Apports acides et cycles des cations  
1040 et de l'azote : quelques reflexions à partir des dispositifs de Monthermé (Ardennes) et d'Aubure  
1041 (Vosges). *Sci. du Sol* 29, 125-145.

1042 Bonneville, S., Bray, A.W., Benning, L.G., 2016. Structural Fe(II) oxidation in biotite by  
1043 an ectomycorrhizal fungi drives mechanical forcing. *Environ. Sci. Technol.* 50, 5589-5596.

1044 Bonneville, S., Smits, M.M., Brown, A., Harrington, J., Leake, J.R., Brydson, R., Benning,  
1045 L.G., 2009. Plant-driven fungal weathering: Early stages of mineral alteration at the nanometer  
1046 scale. *Geology* 37, 615-618.

1047 Brantley, S.L., Liermann, L., Bau, M., Wu, S., 2001. Uptake of trace metals and rare  
1048 earth elements from hornblende by a soil bacterium. *Geomicrobiol. J.*18, 37-61.

1049 Bray, R.J., Curtis, J.T., 1957. An ordination of the upland forest communities in  
1050 southern Wisconsin. *Ecol. Monogr.* 27, 325-349.

1051 Calvaruso, C., Turpault, M.-P., Leclerc, E., Frey-Klett, P., 2007. Impact of  
1052 ectomycorrhizosphere on the functional diversity of soil bacterial and fungal communities from  
1053 a forest stand in relation to nutrient mobilization processes. *Microb. Ecol.* 54, 567-577.

1054 Carroll, S.A., Knauss, K.G., 2005. Dependence of labradorite dissolution kinetics on  
1055 CO<sub>2</sub>(aq), Al(aq), and temperature. *Chem. Geol.* 217, 213-225.

1056 Courty, P.E., Buee, M., Diedhiou, A.G., Frey-Klett, P., Le Tacon, F., Rineau, F.,  
1057 Turpault, M.P., Uroz, S., Garbaye, J., 2010. The role of ectomycorrhizal communities in forest  
1058 ecosystem processes: New perspectives and emerging concepts. *Soil Biol. Biochem.* 42, 679-  
1059 698.

1060 Dambrine, E., Carisey, N., Pollier, B., Granier, A., 1992. Effects of drought on the  
1061 yellowing status and the dynamic of mineral elements in the xylem sap of a declining spruce  
1062 stand (*Picea abies* Karst.). *Plant Soil* 150, 303-306.

1063 Daval, D., Bernard, S., Rémusat, L., Wild, B., Guyot, F., Micha, J.S., Rieutord, F.,  
1064 Magnin, V., Fernandez-Martinez, A., 2017. Dynamics of altered surface layer formation on  
1065 dissolving silicates. *Geochim. Cosmochim. Acta* 209, 51-69.

1066 Daval, D., Calvaruso, C., Guyot, F., Turpault, M.-P., 2018. Time-dependent feldspar  
1067 dissolution rates resulting from surface passivation: Experimental evidence and geochemical  
1068 implications. *Earth Planet. Sci. Lett.*498, 226-236.

1069           Daval, D., Hellmann, R., Saldi, G.D., Wirth, R., Knauss, K.G., 2013. Linking nm-scale  
1070 measurements of the anisotropy of silicate surface reactivity to macroscopic dissolution rate  
1071 laws: New insights based on diopside. *Geochim. Cosmochim. Acta* 107, 121-134.

1072           Daval, D., Sissmann, O., Menguy, N., Saldi, G.D., Guyot, F., Martinez, I., Corvisier, J.,  
1073 Garcia, B., Machouk, I., Knauss, K.G., Hellmann, R., 2011. Influence of amorphous silica layer  
1074 formation on the dissolution rate of olivine at 90°C and elevated pCO<sub>2</sub>. *Chem. Geol.* 284,  
1075 193-209.

1076           Davison, W., Seed, G., 1983. The kinetics of the oxidation of ferrous iron in synthetic  
1077 and natural-waters. *Geochim. Cosmochim. Acta* 47, 67-79.

1078           de Boer, W., Leveau, J.H.J., Kowalchuk, G.A., Gunnewiek, P., Abeln, E.C.A., Figge,  
1079 M.J., Sjollem, K., Janse, J.D., van Veen, J.A., 2004. *Collimonas fungivorans* gen. nov., sp  
1080 nov., a chitinolytic soil bacterium with the ability to grow on living fungal hyphae. *Int. J. Syst.*  
1081 *Evol. Microbiol.* 54, 857-864.

1082           Drever, J.I., Stillings, L.L., 1997. The role of organic acids in mineral weathering.  
1083 *Colloids. Surf. A Physicochem. Eng. Asp.* 120, 167-181.

1084           Duplay, J., Semhi, K., Errais, E., Imfeld, G., Babcsanyi, I., Perrone, T., 2014. Copper,  
1085 zinc, lead and cadmium bioavailability and retention in vineyard soils (Rouffach, France): The  
1086 impact of cultural practices. *Geoderma* 230, 318-328.

1087           El Gh'Mari, A., 1995. Etude minéralogique, pétrophysique et géochimique de la  
1088 dynamique d'altération d'un granite soumis au dépôts atmosphériques acides (Bassin Versant  
1089 du Strengbach, Vosges, France), PhD. Université Louis Pasteur.

1090           Esther, J., Sukla, L.B., Pradhan, N., Panda, S., 2015. Fe (III) reduction strategies of  
1091 dissimilatory iron reducing bacteria. *Korean J. Chem. Eng.* 32, 1-14.

1092 Feger, K.-H., Brahmer, G., Zöttl, H.W., 1990. An integrated watershed/plot-scale study  
1093 of element cycling in spruce ecosystems of the black forest. *Water, Air, Soil Pollut.* 54, 545-  
1094 560.

1095 Ferrier, K.L., Kirchner, J.W., Riebe, C.S., Finkel, R.C., 2010. Mineral-specific chemical  
1096 weathering rates over millennial timescales: Measurements at Rio Icacos, Puerto Rico. *Chem.*  
1097 *Geol.* 277, 101-114.

1098 Fischer, C., Arvidson, R.S., Lüttge, A., 2012. How predictable are dissolution rates of  
1099 crystalline material? *Geochim. Cosmochim. Acta* 98, 177-185.

1100 Frey, B., Rieder, S.R., Brunner, I., Ploetze, M., Koetzsch, S., Lapanje, A., Brandl, H.,  
1101 Furrer, G., 2010. Weathering-associated bacteria from the Damma glacier forefield:  
1102 physiological capabilities and impact on granite dissolution. *Appl. Environ. Microbiol.* 76,  
1103 4788-4796.

1104 Gaillardet, J., Dupre, B., Allegre, C.J., 1995. A global mass budget applied to the Congo  
1105 basin rivers - Erosion rates and continental crust composition. *Geochim. Cosmochim. Acta* 59,  
1106 3469-3485.

1107 Gaillardet, J., Dupré, B., Louvat, P., Allègre, C.J., 1999. Global silicate weathering and  
1108 CO<sub>2</sub> consumption rates deduced from the chemistry of large rivers. *Chem. Geol.* 159, 3-30.

1109 Ganor, J., Renznik, I.J., Rosenberg, Y.O., 2009. Organics in water-rock interactions,  
1110 Thermodynamics and kinetics of water-rock interaction. *Mineralogical Society of America*, pp.  
1111 259-369.

1112 Gerard, F., Clement, A., Fritz, B., Crovisier, J.L., 1996. Introduction of transport  
1113 phenomena into the thermo-kinetic code KINDIS: The code KIRMAT. *C. R. Acad. Sci., Serie*  
1114 *II. Sciences de la Terre et des Planetes* 322, 377-384.

1115           Gin, S., Jegou, C., Frugier, P., Minet, Y., 2008. Theoretical consideration on the  
1116 application of the Aagaard-Helgeson rate law to the dissolution of silicate minerals and glasses.  
1117 Chem. Geol. 255, 14-24.

1118           Gin, S., Jollivet, P., Fournier, M., Angeli, F., Frugier, P., Charpentier, T., 2015. Origin  
1119 and consequences of silicate glass passivation by surface layers. Nat. Commun. 6, 6360.

1120           Gleeson, D.B., Kennedy, N.M., Clipson, N., Melville, K., Gadd, G.M., McDermott,  
1121 F.P., 2006. Characterization of bacterial community structure on a weathered pegmatitic  
1122 granite. Microb. Ecol. 51, 526-534.

1123           Goddéris, Y., Donnadieu, Y., 2009. Climatic plant power. Nature 460, 40.

1124           Godderis, Y., Francois, L.M., Probst, A., Schott, J., Moncoulon, D., Labat, D., Viville,  
1125 D., 2006. Modelling weathering processes at the catchment scale: The WITCH numerical  
1126 model. Geochim. Cosmochim. Acta 70, 1128-1147.

1127           Granier, A., Breda, N., Biron, P., Villette, S., 1999. A lumped water balance model to  
1128 evaluate duration and intensity of drought constraints in forest stands. Ecol. Model. 116, 269-  
1129 283.

1130           Gruber, C., Zhu, C., Georg, R.B., Zakon, Y., Ganor, J., 2014. Resolving the gap between  
1131 laboratory and field rates of feldspar weathering. Geochim. Cosmochim. Acta 147, 90-106.

1132           Gutiérrez, J.L., Jones, C.G., 2006. Physical ecosystem engineers as agents of biogeochemical  
1133 heterogeneity. BioScience 56, 227-236.

1134           Harris, I., Jones, P.D., Osborn, T.J., Lister, D.H., 2014. Updated high-resolution grids  
1135 of monthly climatic observations - the CRU TS3.10 Dataset. Int. J. Climatol. 34, 623-642.

1136           Heckman, K., Welty-Bernard, A., Vazquez-Ortega, A., Schwartz, E., Chorover, J., Rasmussen,  
1137 C., 2013. The influence of goethite and gibbsite on soluble nutrient dynamics and microbial  
1138 community composition. Biogeochemistry 112, 179-195.



1139 Hedrich, S., Schlomann, M., Johnson, D.B., 2011. The iron-oxidizing proteobacteria.  
1140 *Microbiology-Sgm* 157, 1551-1564.

1141 Hellmann, R., Tisserand, D., 2006. Dissolution kinetics as a function of the Gibbs free  
1142 energy of reaction: An experimental study based on albite feldspar. *Geochim. Cosmochim. Acta*  
1143 70, 364-383.

1144 Henri, P.A., Rommevaux-Jestin, C., Lesongeur, F., Mumford, A., Emerson, D.,  
1145 Godfroy, A., Ménez, B., 2016. Structural iron (II) of basaltic glass as an energy source for  
1146 zetaproteobacteria in an abyssal plain environment, off the mid Atlantic ridge. *Front. Microbiol.*  
1147 6.

1148 Johnson, J., Aherne, J., Cummins, T., 2015. Base cation budgets under residue removal  
1149 in temperate maritime plantation forests. *For. Ecol. Manage.* 343, 144-156.

1150 Johnstone, T.C., Nolan, E.M., 2015. Beyond iron: non-classical biological functions of  
1151 bacterial siderophores. *Dalton Trans.* 44, 6320-6339.

1152 Jones, A.A., Bennett, P.C., 2014. Mineral microniches control the diversity of  
1153 subsurface microbial populations. *Geomicrobiol. J.* 31, 246-261.

1154 Jongmans, A.G., vanBreemen, N., Lundstrom, U., vanHees, P.A.W., Finlay, R.D.,  
1155 Srinivasan, M., Unestam, T., Giesler, R., Melkerud, P.A., Olsson, M., 1997. Rock-eating fungi.  
1156 *Nature* 389, 682-683.

1157 Kalinowski, B.E., Liermann, L.J., Brantley, S.L., Barnes, A., Pantano, C.G., 2000. X-  
1158 ray photoelectron evidence for bacteria-enhanced dissolution of hornblende. *Geochim.*  
1159 *Cosmochim. Acta* 64, 1331-1343.

1160 Kim, Y.H., Bae, B., Choung, Y.K., 2005. Optimization of biological phosphorus  
1161 removal from contaminated sediments with phosphate-solubilizing microorganisms. *J. Biosci.*  
1162 *Bioeng.* 99, 23-29.

1163 Klaminder, J., Lucas, R.W., Futter, M.N., Bishop, K.H., Kohler, S.J., Egnell, G.,  
1164 Laudon, H., 2011. Silicate mineral weathering rate estimates: Are they precise enough to be  
1165 useful when predicting the recovery of nutrient pools after harvesting? For. Ecol. Manage. 261,  
1166 1-9.

1167 Knauss, K.G., Wolery, T.J., 1988. The dissolution kinetics of quartz as a function of pH  
1168 and time at 70°C. Geochim. Cosmochim. Acta 52, 43-53.

1169 Lapanje, A., Wimmersberger, C., Furrer, G., Brunner, I., Frey, B., 2012. Pattern of  
1170 elemental release during the granite dissolution can be changed by aerobic heterotrophic  
1171 bacterial strains isolated from Damma glacier (central Alps) deglaciated granite sand. Microb.  
1172 Ecol. 63, 865-882.

1173 Lasaga, A.C., 1998. Kinetic Theory in the Earth Sciences. Princeton University Press,  
1174 New York.

1175 Lefèvre, Y., 1988. Les sols du bassin versant d'Aubure : caractérisation et facteurs de  
1176 répartition. Ann. Sci. For. 45, 417-422.

1177 Lepleux, C., Turpault, M.P., Oger, P., Frey-Klett, P., Uroz, S., 2012. Correlation of the  
1178 abundance of betaproteobacteria on mineral surfaces with mineral weathering in forest soils.  
1179 Appl. Environ. Microbiol. 78, 7114-7119.

1180 Li, Z.B., Liu, L.W., Chen, J., Teng, H.H., 2016. Cellular dissolution at hypha- and spore-  
1181 mineral interfaces revealing unrecognized mechanisms and scales of fungal weathering.  
1182 Geology 44, 319-322.

1183 Lower, S.K., Hochella, M.F., Beveridge, T.J., 2001. Bacterial recognition of mineral  
1184 surfaces: nanoscale interactions between *Shewanella* and  $\alpha$ -FeOOH. Science 292, 1360-1363.

1185 Lucas, R.W., Klaminder, J., Futter, M.N., Bishop, K.H., Egnell, G., Laudon, H.,  
1186 Hogberg, P., 2011. A meta-analysis of the effects of nitrogen additions on base cations:  
1187 Implications for plants, soils, and streams. For. Ecol. Manage. 262, 95-104.

1188 Lüttge, A., Arvidson, R.S., Fischer, C., 2013. A Stochastic Treatment of Crystal  
1189 Dissolution Kinetics. *Elements* 9, 183-188.

1190 Maher, K., DePaolo, D.J., Lin, J.C.-F., 2004. Rates of silicate dissolution in deep-sea  
1191 sediment: In situ measurement using  $^{234}\text{U}/^{238}\text{U}$  of pore fluids. *Geochim. Cosmochim. Acta*  
1192 68, 4629-4648.

1193 Maher, K., Steefel, C.I., White, A.F., Stonestrom, D.A., 2009. The role of reaction  
1194 affinity and secondary minerals in regulating chemical weathering rates at the Santa Cruz Soil  
1195 Chronosequence, California. *Geochim. Cosmochim. Acta* 73, 2804-2831.

1196 Mailloux, B.J., Alexandrova, E., Keimowitz, A.R., Wovkulich, K., Freyer, G.A.,  
1197 Herron, M., Stolz, J.F., Kenna, T.C., Pichler, T., Polizzotto, M.L., Dong, H., Bishop, M.,  
1198 Knappett, P.S.K., 2009. Microbial mineral weathering for nutrient acquisition releases arsenic.  
1199 *Appl. Environ. Microbiol.* 75, 2558-2565.

1200 Mitchell, A.C., Lafreniere, M.J., Skidmore, M.L., Boyd, E.S., 2013. Influence of  
1201 bedrock mineral composition on microbial diversity in a subglacial environment. *Geology* 41,  
1202 855-858.

1203 Negrel, P., Allegre, C.J., Dupre, B., Lewin, E., 1993. Erosion sources determined by  
1204 inversion of major and trace element ratios and strontium isotopic ratios in river water - The  
1205 congo basin case. *Earth Planet. Sci. Lett.* 120, 59-76.

1206 Newman, D.K., Kolter, R., 2000. A role for excreted quinones in extracellular electron  
1207 transfer. *Nature* 405, 94-97.

1208 Nugent, M.A., Brantley, S.L., Pantano, C.G., Maurice, P.A., 1998. The influence of  
1209 natural mineral coatings on feldspar weathering. *Nature* 395, 588-591.

1210 Odum, E.P., 1950. Bird populations of the Highlands (North Carolina) plateau in  
1211 relation to plant succession and avian invasion. *Ecology* 31, 587-605.

1212 Oksanen J., F. Blanchet G., Kindt R., Legendre P., Minchin P. R., O'Hara R. B.,  
1213 Simpson G. L., Solymos P., Stevens M. H. H. and Wagner H. (2013) Vegan: Community  
1214 Ecology Package. R package version 2.0-8, <http://CRAN.R-project.org/package=vegan>.

1215 Or, D., Phutane, S., Dechesne, A., 2007. Extracellular polymeric substances affecting  
1216 pore-scale hydrologic conditions for bacterial activity in unsaturated soils. *Vadose Zone J.* 6,  
1217 298-305.

1218 Paces, T., 1983. Rate constants of dissolution derived from the measurements of mass  
1219 balance in hydrological catchments. *Geochim. Cosmochim. Acta* 47, 1855-1863.

1220 Palandri, J.L., Kharaka, Y.K., 2004. A compilation of rate parameters of water-mineral  
1221 interaction kinetics for application to geochemical modeling, in: Survey, U.S.G. (Ed.), U.S.  
1222 Geological Survey, Open File Report. U.S. Geological Survey, Open File Report, p. 70.

1223 Pierret, M.C., Stille, P., Prunier, J., Viville, D., Chabaux, F., 2014. Chemical and U–Sr  
1224 isotopic variations in stream and source waters of the Strengbach watershed (Vosges mountains,  
1225 France). *Hydrol. Earth Syst. Sci.* 18, 3969-3985.

1226 Reguera, G., McCarthy, K.D., Mehta, T., Nicoll, J.S., Tuominen, M.T., Lovley, D.R.,  
1227 2005. Extracellular electron transfer via microbial nanowires. *Nature* 435, 1098-1101.

1228 Rimstidt, J.D., Brantley, S.L., Olsen, A.A., 2012. Systematic review of forsterite  
1229 dissolution rate data. *Geochim. Cosmochim. Acta* 99, 159-178.

1230 Roden, E.E., Kappler, A., Bauer, I., Jiang, J., Paul, A., Stoesser, R., Konishi, H., Xu,  
1231 H.F., 2010. Extracellular electron transfer through microbial reduction of solid-phase humic  
1232 substances. *Nat. Geosci.* 3, 417-421.

1233 Roelandt, C., Godderis, Y., Bonnet, M.P., Sondag, F., 2010. Coupled modeling of  
1234 biospheric and chemical weathering processes at the continental scale. *Global Biogeochemical*  
1235 *Cycles* 24.

1236 Saha, R., Saha, N., Donofrio, R.S., Bestervelt, L.L., 2013. Microbial siderophores: a  
1237 mini review. *J. Basic Microbiol.* 53, 303-317.

1238 Singh, R., Beriault, R., Middaugh, J., Hamel, R., Chenier, D., Appanna, V.D., Kalyuzhnyi, S.,  
1239 2005. Aluminum-tolerant *Pseudomonas fluorescens*: ROS toxicity and enhanced NADPH  
1240 production. *Extremophiles* 9, 367-373.

1241 Sitch, S., Smith, B., Prentice, I.C., Arneth, A., Bondeau, A., Cramer, W., Kaplan, J.O.,  
1242 Levis, S., Lucht, W., Sykes, M.T., Thonicke, K., Venevsky, S., 2003. Evaluation of ecosystem  
1243 dynamics, plant geography and terrestrial carbon cycling in the LPJ dynamic global vegetation  
1244 model. *Glob. Chang. Biol.* 9, 161-185.

1245 Solden, L., Lloyd, K., Wrighton, K., 2016. The bright side of microbial dark matter:  
1246 lessons learned from the uncultivated majority. *Curr. Opin. Microbiol.* 31, 217-226.

1247 Steefel, C., Lasaga, A.C., 1994. A coupled model for transport of multiple chemical  
1248 species and kinetic precipitation/dissolution reactions with application to reactive flow in single  
1249 phase hydrothermal systems *Am. J. Sci.* 294, 529-592.

1250 Sverdrup, H., 1990. *The kinetics of Chemical Weathering*. Lund University Press, Lund,  
1251 Sweden.

1252 Sverdrup, H., Warfvinge, P., 1993. Calculating field weathering rates using a  
1253 mechanistic geochemical model PROFILE. *Appl. Geochem.* 8, 273-283.

1254 Sverdrup, H., Warfvinge, P., 1995. Estimating field weathering rates using laboratory  
1255 kinetics, *Chemical Weathering Rates of Silicate Minerals*, pp. 485-541.

1256 Taylor, A.S., Blum, J.D., Lasaga, A.C., 2000. The dependence of labradorite dissolution  
1257 and Sr isotope release rates on solution saturation state. *Geochim. Cosmochim. Acta* 64, 2389-  
1258 2400.

1259           Tester, J.W., Worley, W.G., Robinson, B.A., Grigsby, C.O., Feerer, J.L., 1994.  
1260   Correlating quartz dissolution kinetics in pure water from 25 to 625°C. *Geochim. Cosmochim.*  
1261   Acta 58, 2407-2420.

1262           Ullman, W.J., Kirchman, D.L., Welch, S.A., Vandevivere, P., 1996. Laboratory  
1263   evidence for microbially mediated silicate mineral dissolution in nature. *Chem. Geol.* 132, 11-  
1264   17.

1265           Uroz, S., Calvaruso, C., Turpault, M.-P., Frey-Klett, P., 2009. Mineral weathering by  
1266   bacteria: ecology, actors and mechanisms. *Trends Microbiol.* 17, 378-387.

1267           Uroz, S., Calvaruso, C., Turpault, M.P., Pierrat, J.C., Mustin, C., Frey-Klett, P., 2007.  
1268   Effect of the mycorrhizosphere on the genotypic and metabolic diversity of the bacterial  
1269   communities involved in mineral weathering in a forest soil. *Appl. Environ. Microbiol.* 73,  
1270   3019-3027.

1271           Uroz, S., Kelly, L.C., Turpault, M.P., Lepleux, C., Frey-Klett, P., 2015. The  
1272   Mineralosphere concept: mineralogical control of the distribution and function of mineral-  
1273   associated bacterial communities. *Trends Microbiol.* 23, 751-762.

1274           Uroz, S., Turpault, M.P., Delaruelle, C., Mareschal, L., Pierrat, J.C., Frey-Klett, P.,  
1275   2012. Minerals affect the specific diversity of forest soil bacterial communities. *Geomicrobiol.*  
1276   J.29, 88-98.

1277           van der Heijden, G., Legout, A., Pollier, B., Mareschal, L., Turpault, M.P., Ranger, J.,  
1278   Dambrine, E., 2013. Assessing Mg and Ca depletion from broadleaf forest soils and potential  
1279   causes - A case study in the Morvan Mountains. *For. Ecol. Manage.* 293, 65-78.

1280           van Scholl, L., Kuyper, T.W., Smits, M.M., Landeweert, R., Hoffland, E., van Breemen,  
1281   N., 2008. Rock-eating mycorrhizas: their role in plant nutrition and biogeochemical cycles.  
1282   *Plant Soil* 303, 35-47.

1283 Vassilev, N., Vassileva, M., Nikolaeva, I., 2006. Simultaneous P-solubilizing and  
1284 biocontrol activity of microorganisms: potentials and future trends. *Appl. Microbiol.*  
1285 *Biotechnol.* 71, 137-144.

1286 Violette, A., Godd ris, Y., Mar chal, J.-C., Riotte, J., Oliva, P., Kumar, M.S.M., Sekhar,  
1287 M., Braun, J.-J., 2010. Modelling the chemical weathering fluxes at the watershed scale in the  
1288 Tropics (Mule Hole, South India): Relative contribution of the smectite/kaolinite assemblage  
1289 versus primary minerals. *Chem. Geol.* 277, 42-60.

1290 Viville, D., Chabaux, F., Stille, P., Pierret, M.C., Gangloff, S., 2012. Erosion and  
1291 weathering fluxes in granitic basins: The example of the Strengbach catchment (Vosges massif,  
1292 eastern France). *Catena* 92, 122-129.

1293 Walters, W.A., Caporaso, J.G., Lauber, C.L., Berg-Lyons, D., Fierer, N., Knight, R.,  
1294 2011. PrimerProspector: de novo design and taxonomic analysis of barcoded polymerase chain  
1295 reaction primers. *Bioinformatics* 27, 1159-1161.

1296 Ward, J.H., 1963. Hierarchical Grouping to Optimize an Objective Function. *J. Am.*  
1297 *Stat. Assoc.* 58, 236-244.

1298 Warfvinge, P., Sverdrup, H., 1988. Soil liming as a measure to mitigate acid  
1299 runoff. *Water Resour. Res.* 24, 701-712.

1300 Warfvinge, P., Sverdrup, H., 1992. Calculating critical loads of acid deposition with  
1301 PROFILE - a steady-state soil chemistry model. *Water, Air, Soil Pollut.* 63, 119-143.

1302 Weber, K.A., Achenbach, L.A., Coates, J.D., 2006. Microorganisms pumping iron:  
1303 anaerobic microbial iron oxidation and reduction. *Nat. Rev. Microbiol.* 4, 752-764.

1304 Welch, S.A., Barker, W.W., Banfield, J.F., 1999. Microbial extracellular  
1305 polysaccharides and plagioclase dissolution. *Geochim. Cosmochim. Acta* 63, 1405-1419.

1306 Welch, S.A., Ullman, W.J., 1993. The effect of organic acids on plagioclase dissolution  
1307 rates and stoichiometry. *Geochim. Cosmochim. Acta* 57, 2725-2736.

1308 White, A.F., Brantley, S.L., 2003. The effect of time on the weathering of silicate  
1309 minerals: why do weathering rates differ in the laboratory and field? *Chem. Geol.* 202, 479-  
1310 506.

1311 Wild, B., Daval, D., Guyot, F., Knauss, K.G., Pollet-Villard, M., Imfeld, G., 2016. pH-  
1312 dependent control of feldspar dissolution rate by altered surface layers. *Chem. Geol.* 442, 148-  
1313 159.

1314 Wild, B., Imfeld, G., Guyot, F., Daval, D., 2018. Early stages of bacterial community  
1315 adaptation to silicate aging. *Geology* 46, 555-558.

1316 Wu, L., Jacobson, A.D., Chen, H.-C., Hausner, M., 2007. Characterization of elemental  
1317 release during microbe-basalt interactions at T=28 degrees C. *Geochim. Cosmochim. Acta* 71,  
1318 2224-2239.

1319 Wu, L., Jacobson, A.D., Hausner, M., 2008. Characterization of elemental release  
1320 during microbe-granite interactions at T=28 °C. *Geochim. Cosmochim. Acta* 72, 1076-1095.

1321 Yarza, P., Yilmaz, P., Pruesse, E., Glockner, F.O., Ludwig, W., Schleifer, K.-H.,  
1322 Whitman, W.B., Euzéby, J., Amann, R., Rossello-Mora, R., 2014. Uniting the classification of  
1323 cultured and uncultured bacteria and archaea using 16S rRNA gene sequences. *Nat. Rev.*  
1324 *Microbiol.* 12, 635-645.

1325 Yeh, G.T., Tripathi, V.S., 1991. A Model for Simulating Transport of Reactive  
1326 Multispecies Components: Model Development and Demonstration. *Water Resour. Res.* 27,  
1327 3075-3094.

1328 Yu, C., Lavergne, U., Peltola, P., Drake, H., Bergbäck, B., Åström, M.E., 2014.  
1329 Retention and transport of arsenic, uranium and nickel in a black shale setting revealed by a  
1330 long-term humidity cell test and sequential chemical extractions. *Chem. Geol.* 363, 134-144.



1331 Zhu, C., Liu, Z., Schaefer, A., Wang, C., Zhang, G., Gruber, C., Ganor, J., Georg, R.B.,  
1332 2014. Silicon Isotopes as a New Method of Measuring Silicate Mineral Reaction Rates at  
1333 Ambient Temperature. *Procedia Earth and Planet. Sci.* 10, 189-193.

1334

1335

## 1336 **8. FIGURE CAPTIONS**

1337

1338 Fig. 1: Compartments of the critical zone probed at the Strengbach catchment (A). Soil profile  
1339 of the beech plot (B) and corresponding reactivity probes after 20 months of incubation into the  
1340 A horizon (C) and the C horizon (D). Overview of the setup used to expose samples to  
1341 atmospheric weathering (E) onto a Polytetrafluoroethylene (PTFE) plate (F). Reactivity probe  
1342 after 20 months of incubation at the weather station (G). Experimental setup used to immerse  
1343 samples into the Strengbach stream at the outlet (H) with flow-through PTFE holders (I).  
1344 Reactivity probe after 20 months of incubation into the Strengbach stream (J). White and black  
1345 crosses indicate the locations of the samples.

1346

1347 Fig. 2: Exchangeable Mg (A) and Ca (B) as determined by ammonium acetate extractions on  
1348 samples of the soil profile of the beech plot collected on 11/18/2013 and 12/02/2014 (see Table  
1349 A.3). For comparison, green and orange plots represent corresponding concentrations measured  
1350 at the experimental plot of Breuil-Chenue (Morvan, France) before and 30 years after  
1351 deforestation respectively (van der Heijden *et al.*, 2013).

1352

1353 Fig. 3: Labradorite sample collected after 9 months of incubation in the C horizon of the soil  
1354 profile of the beech plot at the Strengbach catchment. Stereo microscope image acquired before  
1355 removal of the Room Temperature Vulcanizing (RTV) glue mask (A), vertical scanning

1356 interferometry (VSI) surface topography after cleaning (B) and interpretation in terms of  
1357 surface retreat overlaid on stitched VSI images before removal of the RTV glue mask  
1358 (visible inside the circled area) of the same portion of the sample (C). Black arrowheads in (B)  
1359 indicate zones where the global retreat of the surface at the previous location of the mask is  
1360 visible. White arrows indicate another boundary of the mask indicated by a residue of RTV  
1361 glue. Striped zone in (C) correspond to a location where natural fluid circulation likely occurred  
1362 (see text).

1363

1364 Fig. 4: Olivine samples after 9 months of incubation in the A horizon of the soil profile of the  
1365 beech plot at the Strengbach catchment. Stereo microscope image acquired before removal of  
1366 the RTV glue mask (A) and stitched VSI images of the surface after cleaning (B). Dashed lines  
1367 indicate the boundary of zones interpreted in (C) as portions of the olivine surface that were  
1368 either masked (1), including traces of possible fluid circulation (2), or the rest of the mineral  
1369 surface exposed to the soil environment (3). Red box in C indicates the portion of the surface  
1370 imaged by stereo microscope right after incubation (D) or by VSI before (E) and after (F) 9  
1371 months of incubation. Striped zone in (D), (E) and (F) correspond to the masked area. Profiles  
1372 at the boundary between zones 2 and 3 and zones 1 and 2 (indicated by a red arrowhead) before  
1373 (in blue) and after (in red) 9 months of incubation are reported in (G) and (H) respectively..

1374

1375 Fig. 5: Detail of the surface topography of an olivine reactivity probe before (A) and after (B)  
1376 9 months of incubation in the A horizon of the soil profile at the beech plot. Superposition of  
1377 profiles before (black) and after (red) incubation (C) and corresponding surface retreat (D). This  
1378 analysis reveals a global retreat of the surface (red arrow, C; dashed area, D) and local alteration  
1379 features (green arrow, C; dotted area, D).

1380

1381 Fig. 6: Detail of the surface topography of an olivine reactivity probe after 9 months of  
1382 incubation in the A horizon of the soil profile of the  
1383 plot (A, C). Its interpretation in terms of weathering fluxes, as estimated from topography and  
1384 rate spectra (D, E) following the approach developed in (Fischer et al., 2012), is displayed (B).  
1385 It reveals zones impacted by the global retreat of the surface (green) with respect to the initial  
1386 masked surface area (black, M) and local alteration features (red). The contribution of zones  
1387 related to the initial topography is highlighted in grey.

1388

1389 Fig. 7: Temporal variations of pH (A), temperature (B), and dissolution rates (C) of olivine and  
1390 labradorite modeled by WITCH for two soil horizons at the beech plot of the Strengbach  
1391 catchment. The greyed areas correspond to the incubation period of the probes.

1392

1393 Fig. 8: Relative proportions of bacterial phyla analyzed in the environmental probes incubated  
1394 in several compartments of the critical zone at the Strengbach catchment. Mean values over all  
1395 samples incubated at a given location. “Others” category gathers the 20 less represented phyla  
1396 together with sequences which could not be classified with a sufficient degree of confidence.

1397

1398 Fig. 9: Statistical analyses of the composition of microbial communities of the environmental  
1399 probes incubated at the weather station (A,B), in the A horizon (C,D), in the C horizon (E,F),  
1400 and in the stream (G,H). Analyzed samples include the mineralosphere of labradorite (L),  
1401 olivine (O) and quartz (Q), as well as microbial communities from environmental matrices (E,  
1402 either soil or stream sediments) and empty test bags (B). Trees correspond to the aggregation  
1403 of OTUs at the species level with the Ward method on the basis of Bray-Curtis distances (A, C,  
1404 E, G). Principal coordinate analyses (PCoA) of the relative abundance of the 16S rRNA genes  
1405 with colors corresponding to the clusters determined with the Ward method. Crosses match to

1406 *a posteriori* projection of OTUs corresponding to *Collimonas* sp. (1), *Burkholderia* sp. (2),  
1407 *Pseudomonas* sp. (3), *Janthinobacterium* sp. (4), *Leifsonia* sp. (5), *Polaromonas* sp. (6),  
1408 *Sphingomonas* sp. (7), *Arthrobacter* sp. (8).

1409

1410 Fig. 10: Detail of the surface topography of an olivine reactivity probe before (A) and after (B)  
1411 20 months of incubation at the weather station. Superposition of profiles before (black) and  
1412 after (red) incubation (C) and corresponding surface retreat (D). 3D plot of the surface after  
1413 incubation (B) with masked (M) zones (E).

1414

1415 Fig. 11: Evolutions of the  $f(\Delta G_r)$  term, which describes the effect of the distance from  
1416 equilibrium of the solution on mineral dissolution rate, and of the surface retreats for olivine  
1417 and labradorite predicted by the WITCH model for the A and C horizons of the soil profile (A).  
1418 The period highlighted in grey corresponds to the incubation of the samples. The  $f(\Delta G_r)$   
1419 function is equal to  $\sim 1$  for all conditions except for labradorite in the C horizon when the *rate* –  
1420  $\Delta G_r$  relation is described by the model of Taylor *et al.* (2000). Squares and diamonds in panels  
1421 (B)-(D) represent *measured* surface retreats for samples incubated in the A and C horizons,  
1422 respectively. Continuous curves represent *predicted* surface retreats based on outputs from the  
1423 WITCH model. Corrected curves take into account fluid-mineral contact time and are based on  
1424 ( $f_2(\Delta G_r)$ ) function (see text). This figure stresses the amplitude of the field-laboratory  
1425 discrepancy. The error bars are smaller than the size of symbols.

1426

1427 Fig. 12: Relative proportions of *Pseudomonas* sp., *Burkholderia* sp., *Collimonas* sp. (A), and  
1428 *Arthrobacter* sp., *Leifsonia* sp., *Janthinobacterium* sp., et *Polaromonas* sp. (B), in the  
1429 mineralospheres of quartz (Q), labradorite (L) and olivine (O), as well as in environmental  
1430 samples (E) or empty bags (B). This figure illustrates that the proportion of genera known for

1431 their mineral weathering ability in pedological context is increased in the microbial  
1432 communities of the environmental probes compared to those recovered from their respective  
1433 surrounding environmental matrix.

1434

## 1435 **9. TABLE CAPTIONS**

1436

1437 Table 1: Global retreat of the surface of labradorite  $\Delta_z$  and associated dissolution rate  $r$   
1438 measured *in-situ* in the field ( $F$ ) or issued from WITCH simulations from kinetic rate laws  
1439 determined in the laboratory ( $L$ ), based on the transition state theory. Values between  
1440 parentheses are based on a rate -  $\Delta G_r$  relationship by Taylor *et al.* (2000). Predicted extent of  
1441 reaction  $\xi$  and associated field-laboratory discrepancies  $\Delta_{L/F}$ . n.d. could not be estimated based  
1442 on the methodology proposed here, since expected retreats were lower than measurable retreats  
1443 due to the quality of the polishing of the corresponding samples.

1444

1445 Table 2: Global retreat of the surface of olivine  $\Delta_z$  and associated dissolution rate  $r$  measured  
1446 *in-situ* in the field ( $F$ ) or issued from WITCH simulations from kinetic rate laws determined in  
1447 the laboratory ( $L$ ), based on the transition state theory. Predicted extent of reaction  $\xi$  and  
1448 associated field-laboratory discrepancies  $\Delta_{L/F}$ . \* retreat determined on a zone with no specific  
1449 feature proving fluid circulation. \*\* possibly of biotic origin (see text).

Table 1

Sample	Context	incubation duration [months]	Labradorite							
			$\Delta_Z^F$ [nm]	$r_F$ [mol.m <sup>-2</sup> .s <sup>-1</sup> ]	T [°C]	pH	$\Delta_Z^L$ [nm]	$r_L$ [mol.m <sup>-2</sup> .s <sup>-1</sup> ]	$\xi$ [mol.m <sup>-2</sup> ]	$\Delta_{L/F}$
ML9	Weather Station	9	2*	8.59E-13	7.1	5.4	4.4	1.88E-12	4.49E-05	2.2
ML20	Weather Station	20	2*	3.84E-13	7.1	5.4	9.8	1.88E-12	1.01E-04	4.9
AL9a	A horizon	9	2*	8.59E-13	6.1	4.2	30.6	1.31E-11	2.93E-04	15.3
AL9b	A horizon	9	4.5	1.99E-12	6.1	4.2	30.3	1.34E-11	2.87E-04	6.7
AL20	A horizon	20	1.1*	2.11E-13	6.1	4.2	59.4	1.14E-11	5.68E-04	54.0
CL9a	C horizon	9	1.5*	6.44E-13	6.1	5.2	6.2 (1.7)	2.68E-12 (7.24E-13)	3.26E-05	4.1 (1.1)
CL9b	C horizon	9	1*	4.42E-13	6.1	5.2	6.1 (1.6)	2.72E-12 (7.24E-13)	3.16E-05	6.1 (1.6)
CL9c	C horizon	9	2.5*	1.11E-12	6.1	5.2	6.1 (1.6)	2.72E-12 (7.24E-13)	3.16E-05	2.4 (0.7)
CL20	C horizon	20	1.5*	2.88E-13	6.1	5.2	11.2 (3.1)	2.17E-12 (5.85E-13)	5.95E-05	7.5 (2.0)
EL9a	Stream	9	5*	2.15E-12	5.8	6.5	0.8	3.55E-13	8.45E-06	n.d.
EL9b	Stream	9	4*	1.77E-12	5.8	6.5	0.8	3.55E-13	8.21E-06	n.d.
EL20	Stream	20	1*	1.92E-13	5.8	6.5	1.8	3.55E-13	1.89E-05	1.8

Table 2

Sample	Context	incubation duration [months]	Olivine							
			$\Delta_Z^F$ [nm]	$r_F$ [mol.m <sup>-2</sup> .s <sup>-1</sup> ]	T [°C]	pH	$\Delta_Z^L$ [nm]	$r_L$ [mol.m <sup>-2</sup> .s <sup>-1</sup> ]	$\xi$ [mol.m <sup>-2</sup> ]	$\Delta_{L/F}$
MO9	Weather Station	9	1*	9.38E-13	7.1	5.4	83.8	7.87E-11	1.70E-03	84
MO20	Weather Station	20	171	7.17E-11	7.1	5.4	187.7	7.87E-11	3.82E-03	1
AO9	A horizon	9	24.19	2.27E-11	6.1	4.2	407.2	3.82E-10	8.53E-03	17
AO20	A horizon	20	3**	1.26E-12	6.1	4.2	809.6	3.39E-10	1.71E-02	270
CO9	C horizon	9	1.5	1.41E-12	6.1	5.2	112.1	1.05E-10	1.48E-03	75
CO20	C horizon	20	2*	8.38E-13	6.1	5.2	211.1	8.85E-11	2.75E-03	106
EO9	Stream	9	2.5	2.35E-12	5.8	6.5	21.7	2.04E-11	4.53E-04	9
EO20	Stream	20	2.5*	1.05E-12	5.8	6.5	48.6	2.04E-11	1.01E-03	19

Figure 1

[Click here to download high resolution image](#)

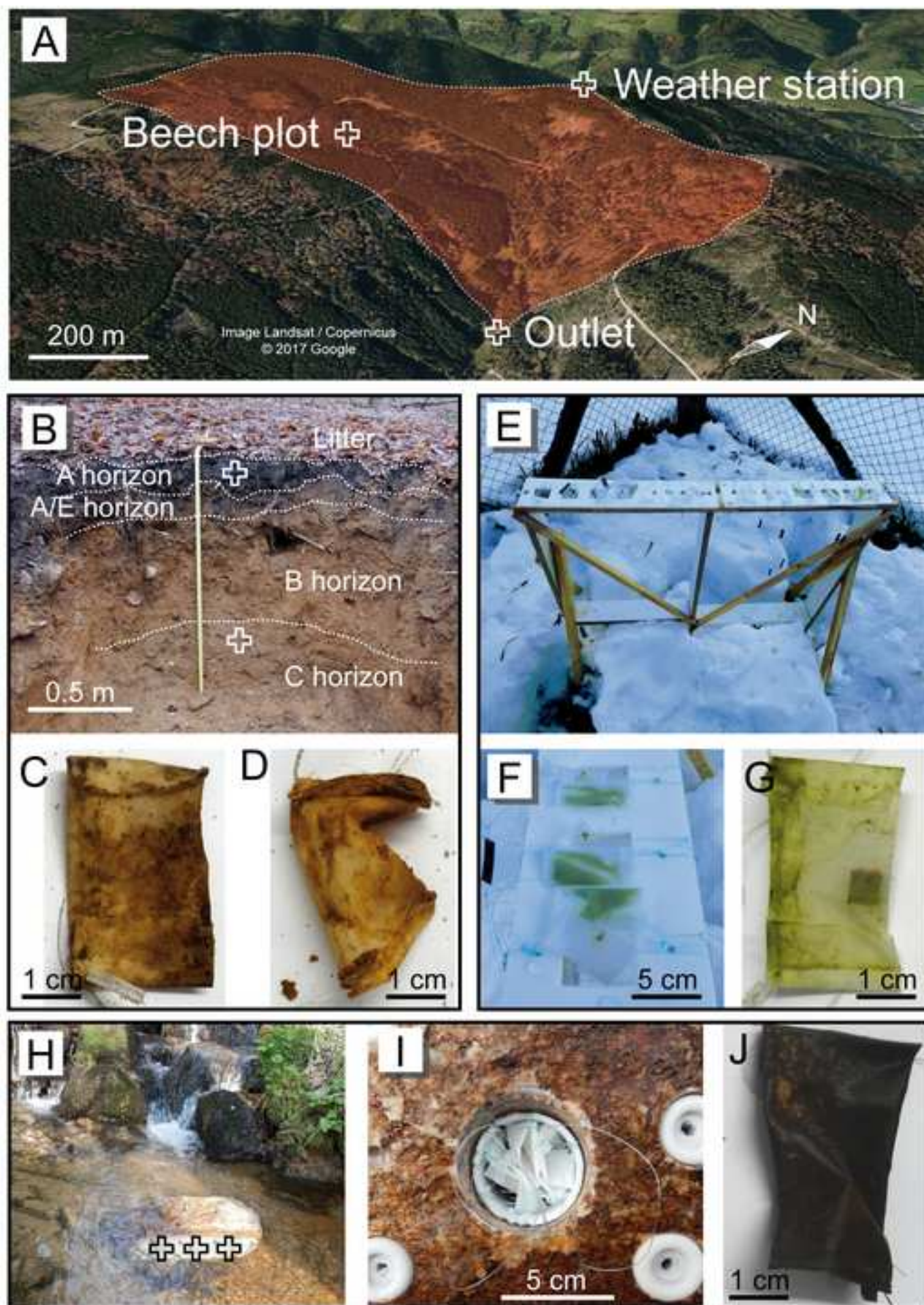
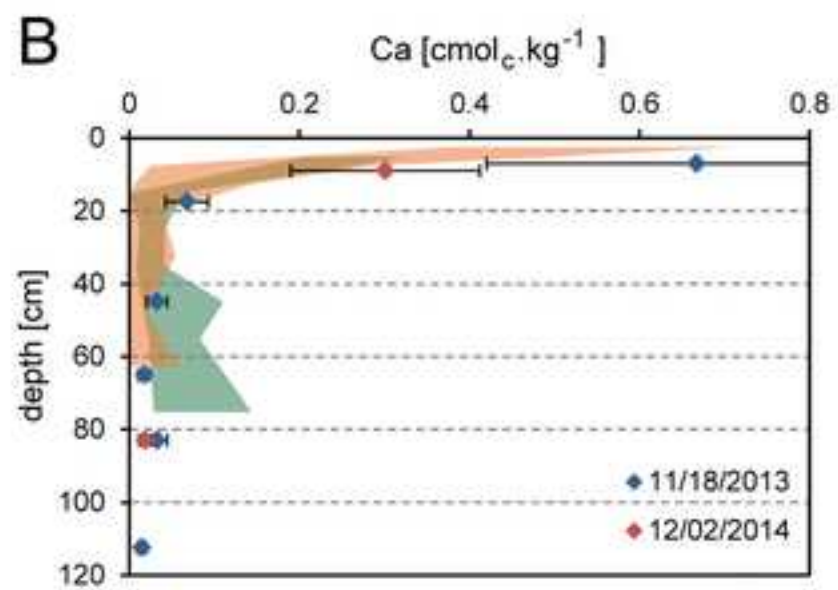
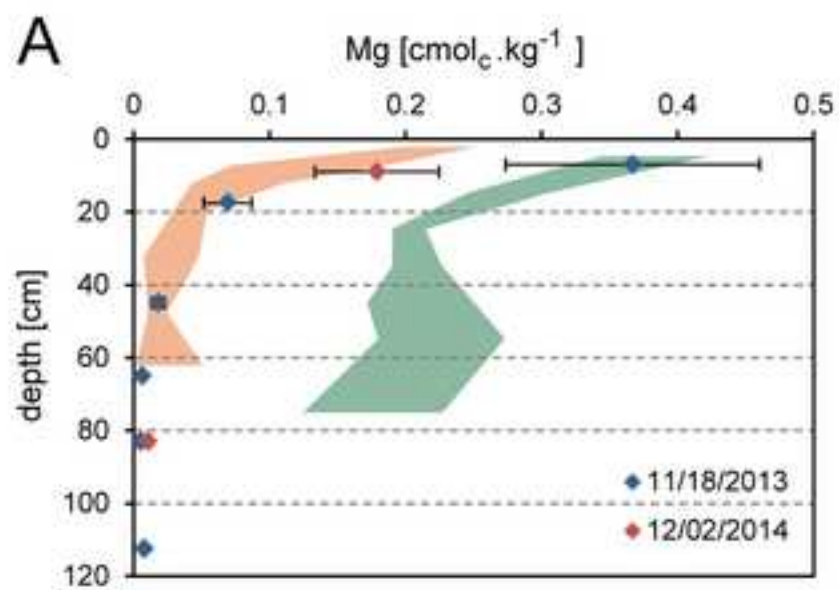




Figure 2  
[Click here to download high resolution image](#)



**Figure 3**  
[Click here to download high resolution image](#)

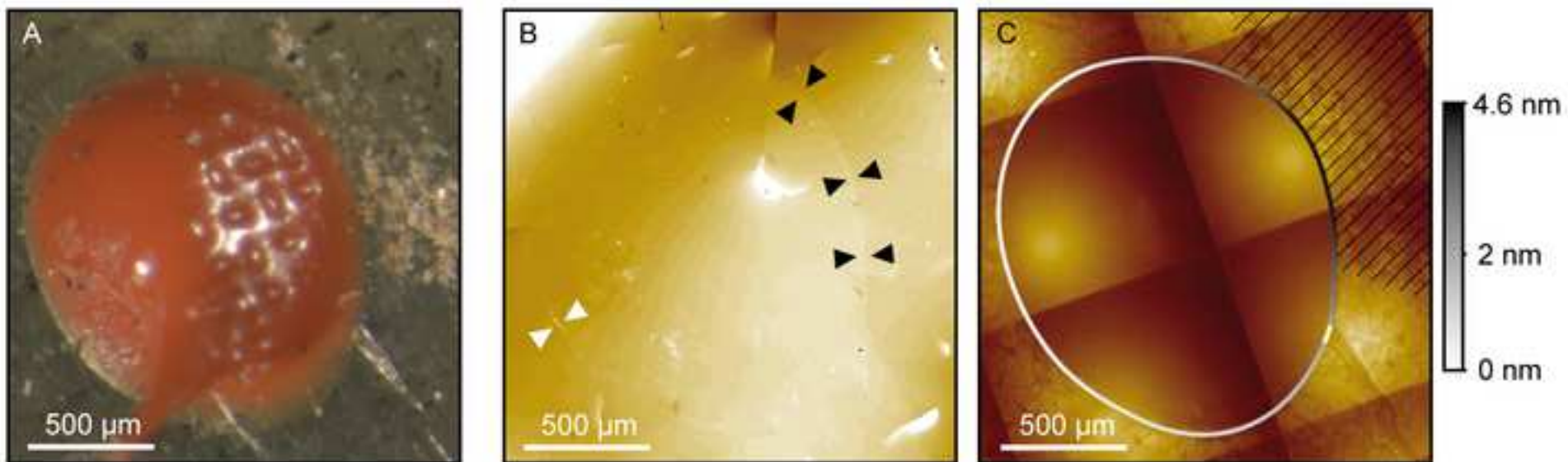


Figure 4  
[Click here to download high resolution image](#)

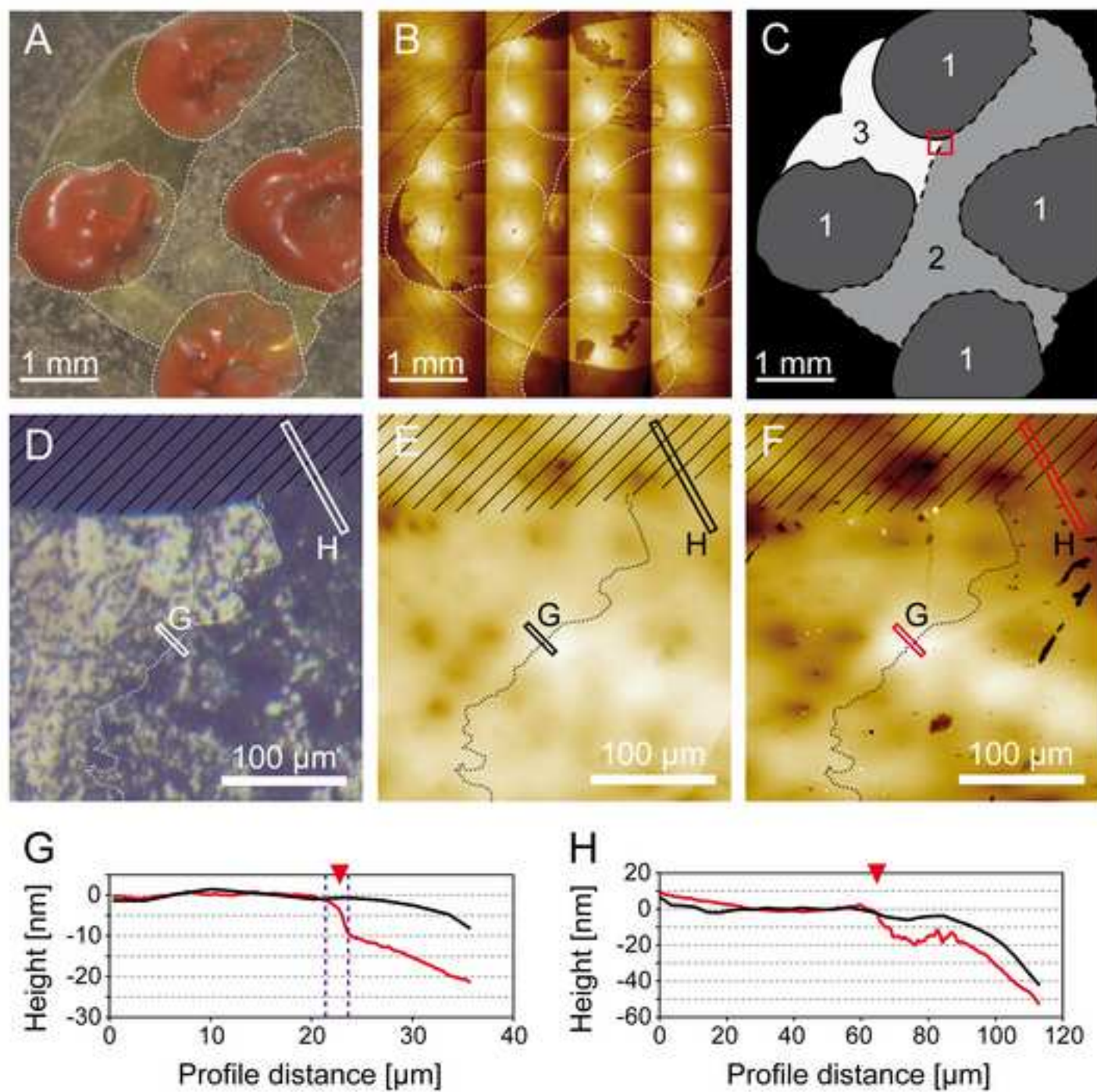


Figure 5  
[Click here to download high resolution image](#)

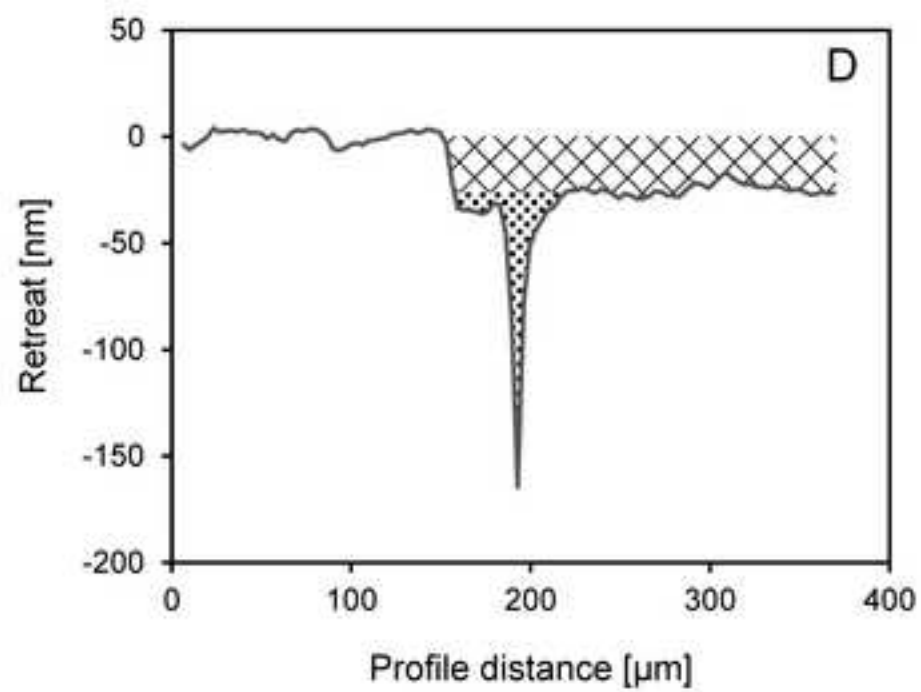
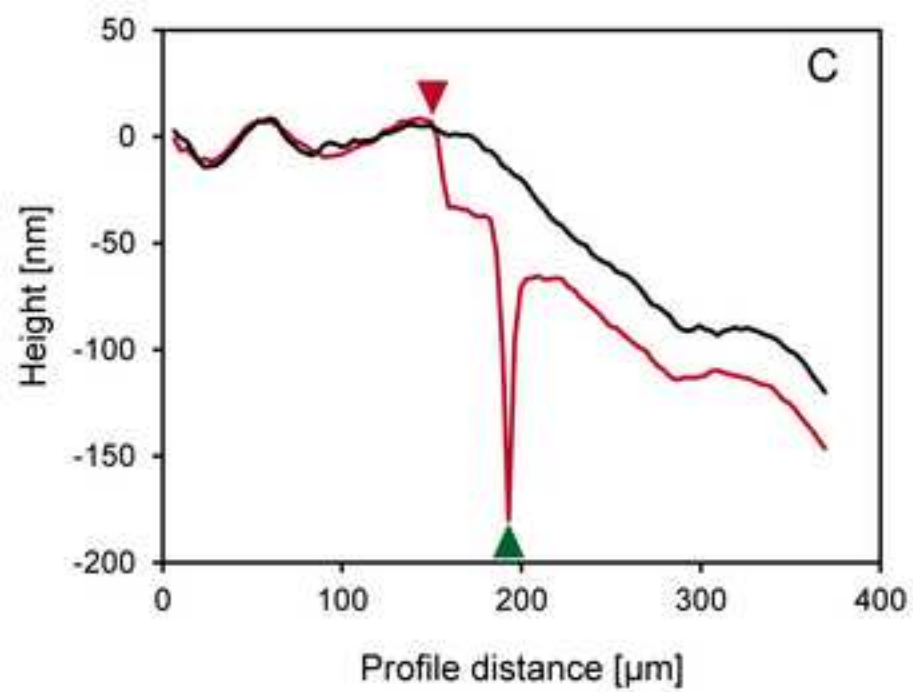
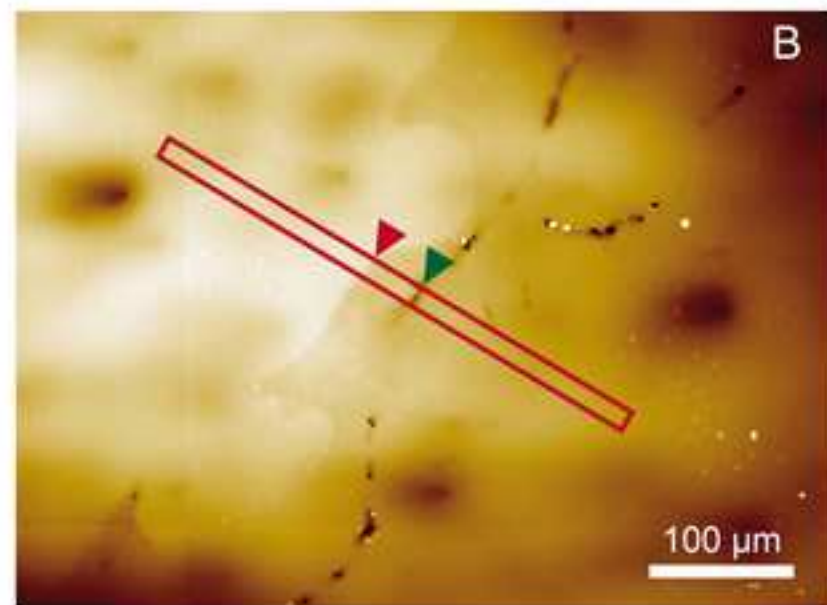
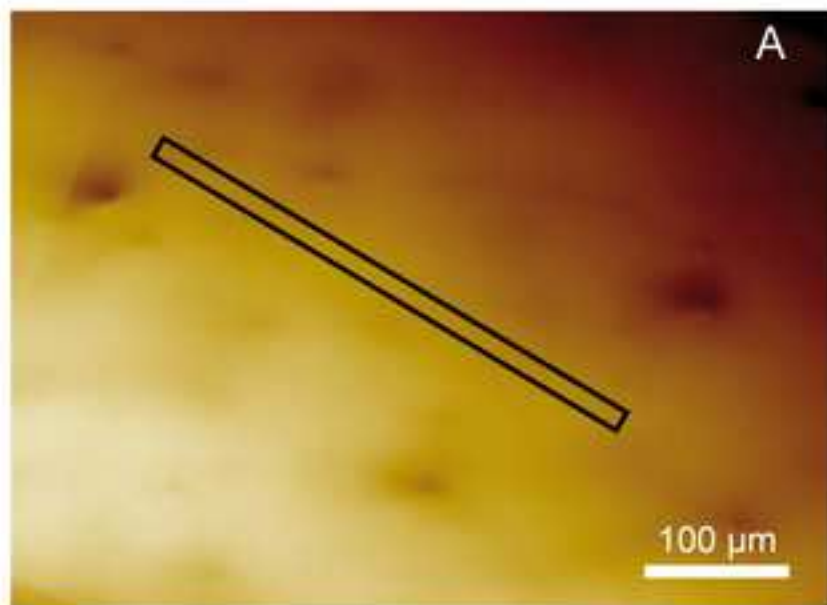




Figure 6  
[Click here to download high resolution image](#)

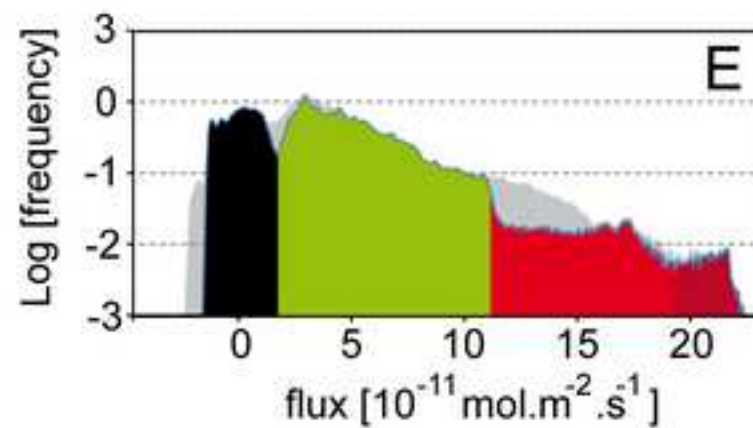
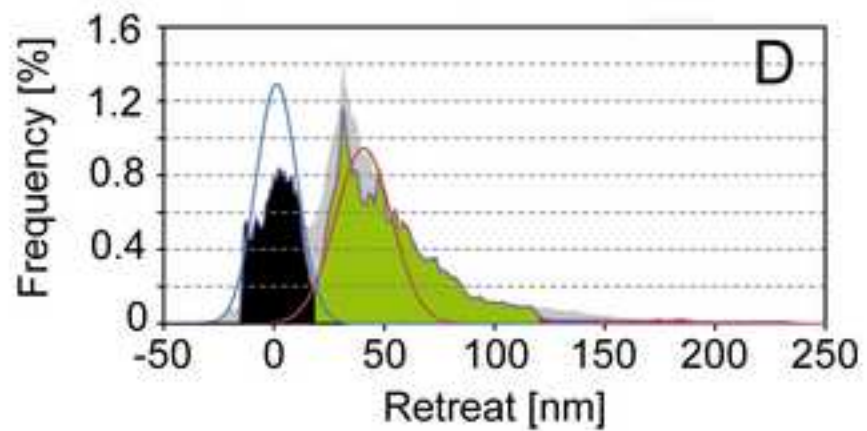
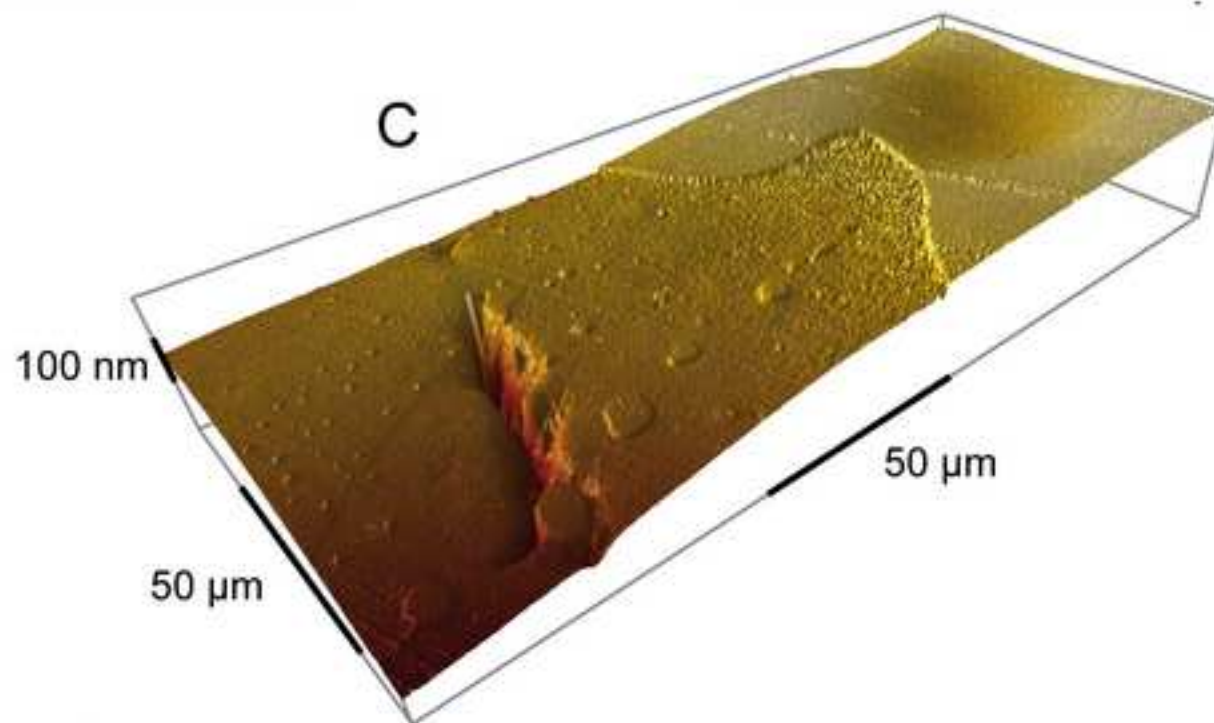


Figure 7

[Click here to download high resolution image](#)

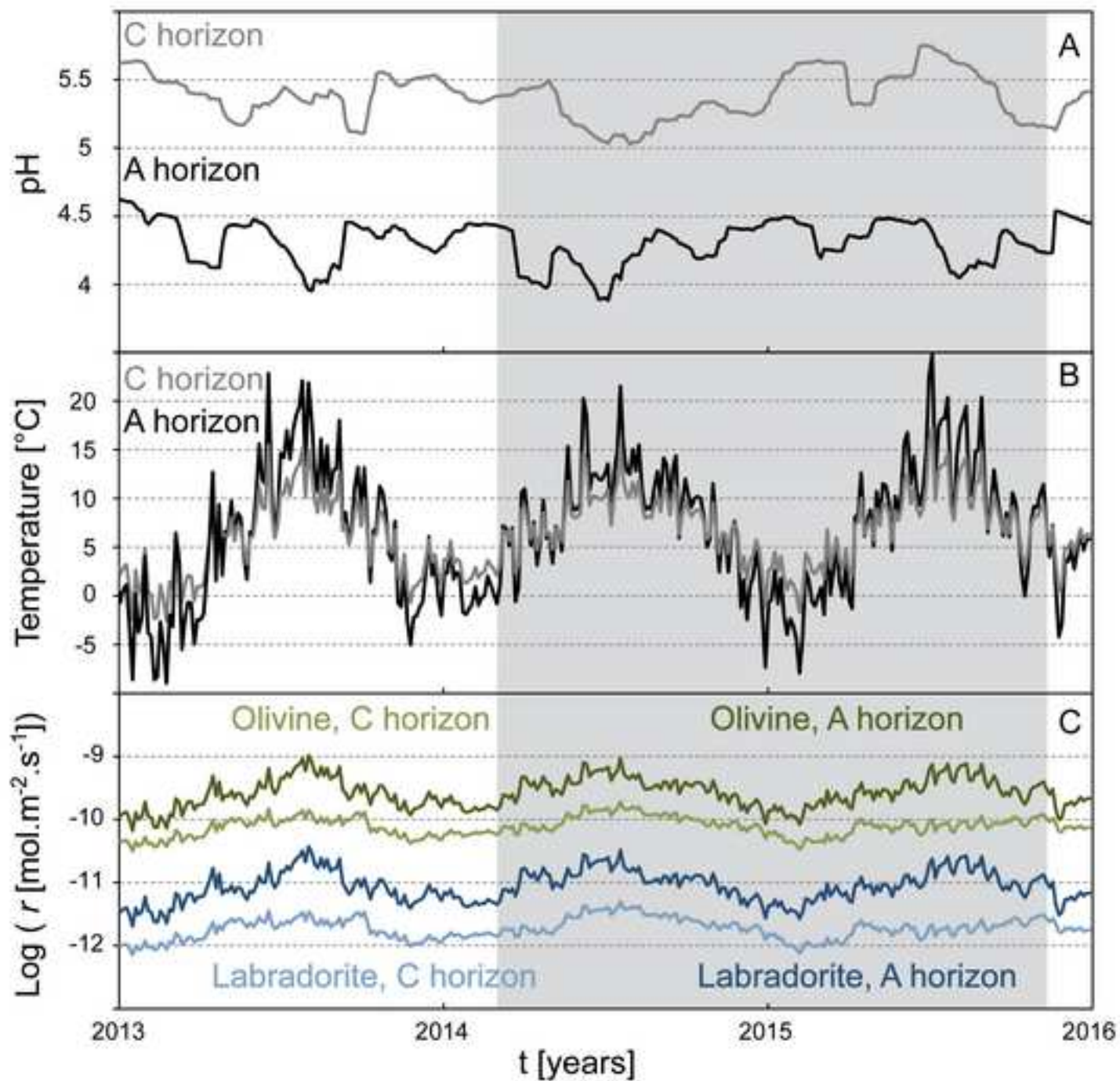


Figure 8  
[Click here to download high resolution image](#)

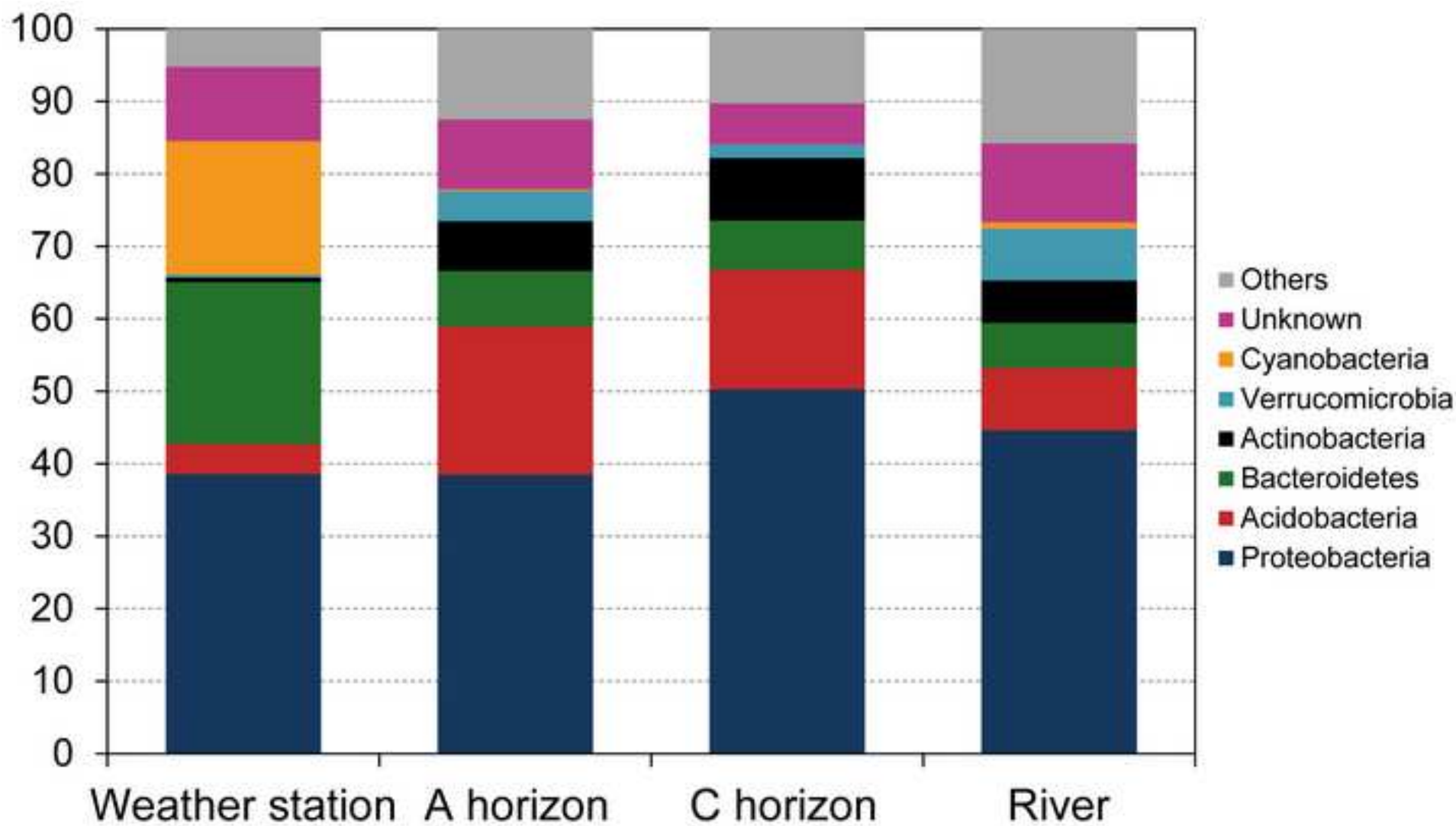


Figure 9

[Click here to download high resolution image](#)

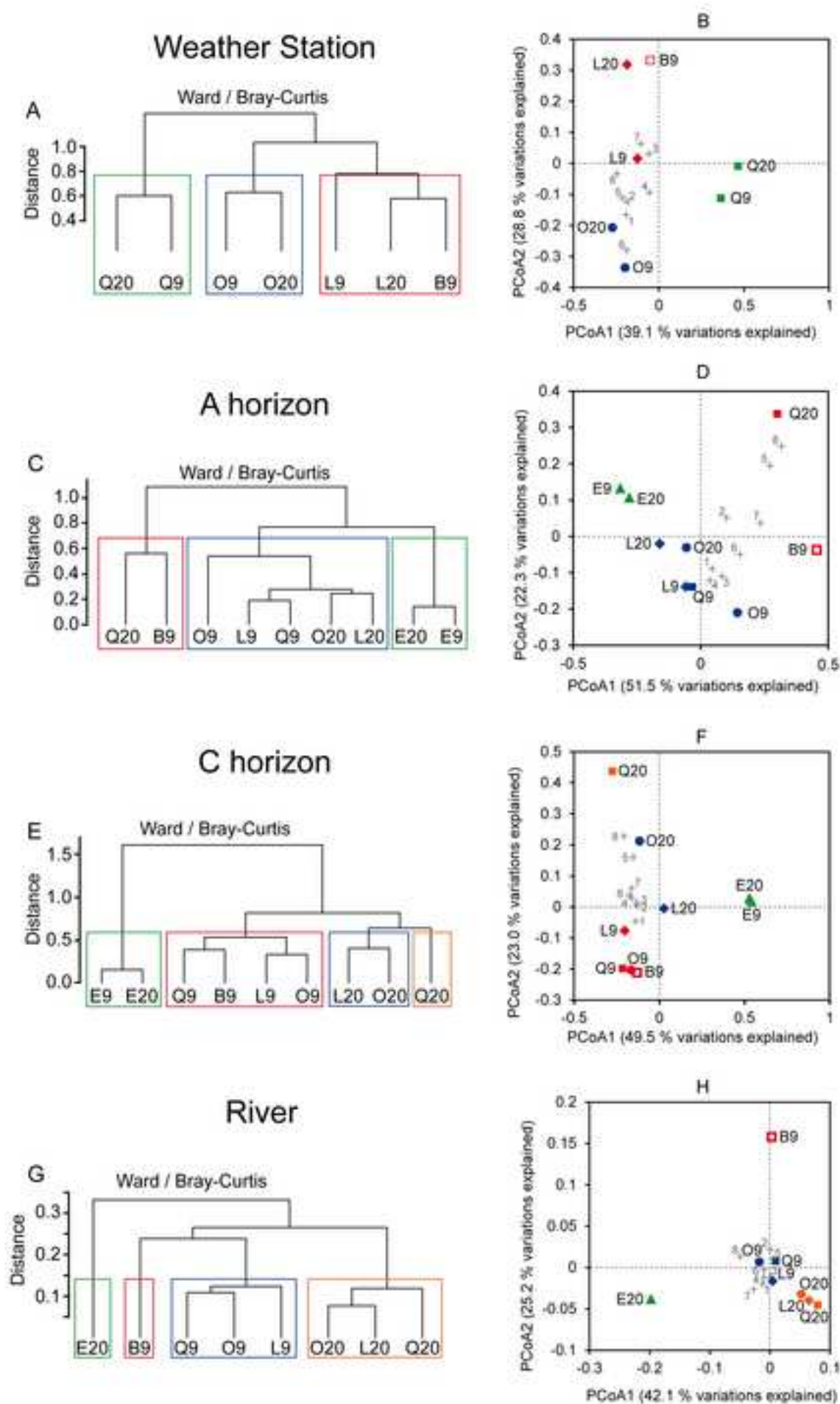




Figure 10  
[Click here to download high resolution image](#)

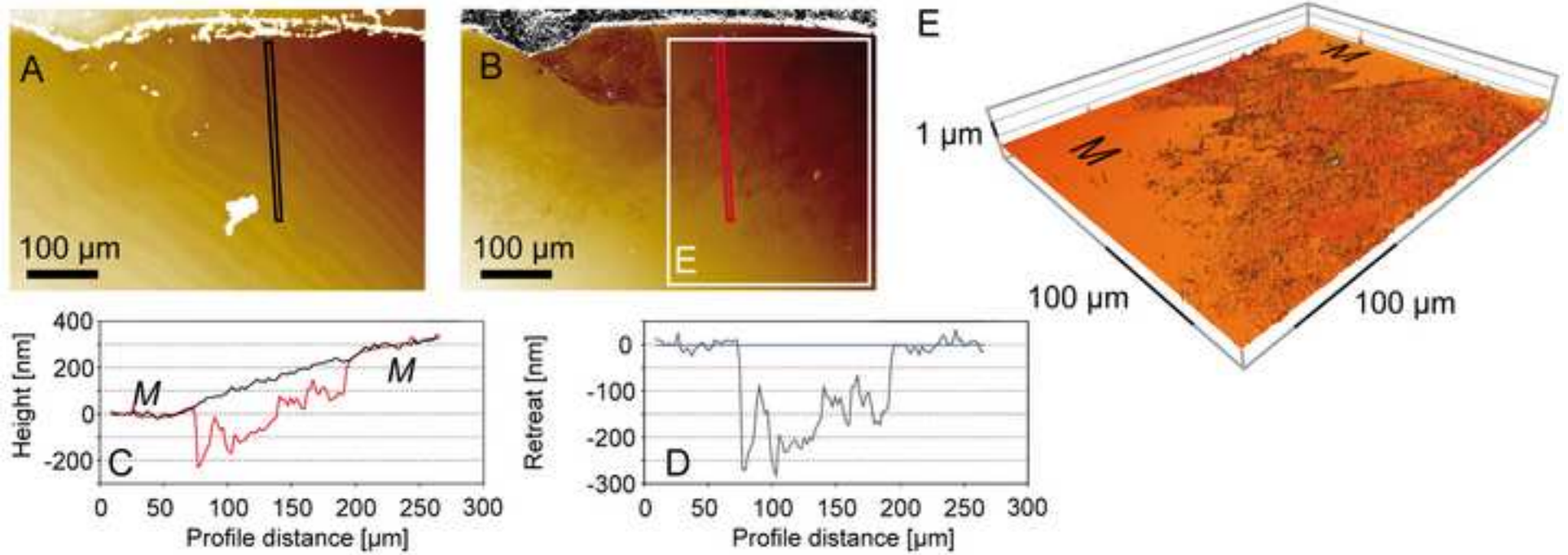


Figure 11  
[Click here to download high resolution image](#)

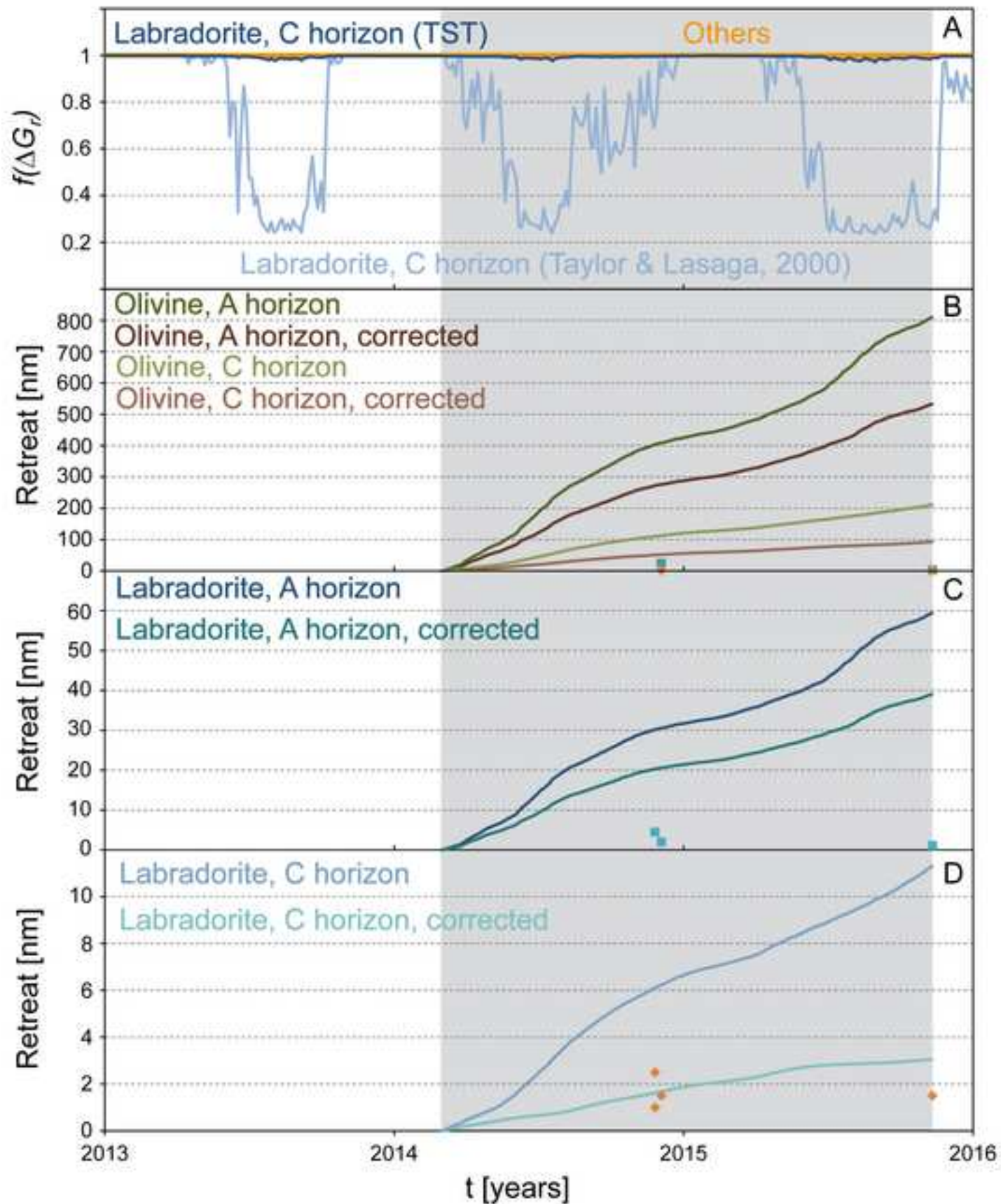


Figure 12

[Click here to download high resolution image](#)

